



## Shape evolution of neutron-rich $^{106,108,110}\text{Mo}$ isotopes in the triaxial degree of freedom

J. Ha, T. Sumikama, F. Browne, N. Hinohara, A.M. Bruce, S. Choi, I. Nishizuka, S. Nishimura, P. Doornenbal, G. Lorusso, et al.

### ► To cite this version:

J. Ha, T. Sumikama, F. Browne, N. Hinohara, A.M. Bruce, et al.. Shape evolution of neutron-rich  $^{106,108,110}\text{Mo}$  isotopes in the triaxial degree of freedom. *Phys.Rev.C*, 2020, 101 (4), pp.044311. 10.1103/PhysRevC.101.044311 . hal-02564650

**HAL Id: hal-02564650**

**<https://hal.science/hal-02564650>**

Submitted on 21 Dec 2020

**HAL** is a multi-disciplinary open access archive for the deposit and dissemination of scientific research documents, whether they are published or not. The documents may come from teaching and research institutions in France or abroad, or from public or private research centers.

L'archive ouverte pluridisciplinaire **HAL**, est destinée au dépôt et à la diffusion de documents scientifiques de niveau recherche, publiés ou non, émanant des établissements d'enseignement et de recherche français ou étrangers, des laboratoires publics ou privés.

# Shape evolution of neutron-rich $^{106,108,110}\text{Mo}$ isotopes in the triaxial degree of freedom

J. Ha,<sup>1,2,\*</sup> T. Sumikama,<sup>2,3,†</sup> F. Browne,<sup>2,4</sup> N. Hinohara,<sup>5,6</sup> A. M. Bruce,<sup>4</sup> S. Choi,<sup>1</sup> I. Nishizuka,<sup>3</sup> S. Nishimura,<sup>2</sup> P. Doornenbal,<sup>2</sup> G. Lorusso,<sup>2,7,8</sup> P.-A. Söderström,<sup>2</sup> H. Watanabe,<sup>2,9</sup> R. Daido,<sup>10</sup> Z. Patel,<sup>2,7</sup> S. Rice,<sup>2,7</sup> L. Sinclair,<sup>2,11</sup> J. Wu,<sup>2,12</sup> Z. Y. Xu,<sup>13,14</sup> A. Yagi,<sup>10</sup> H. Baba,<sup>2</sup> N. Chiga,<sup>3,2</sup> R. Carroll,<sup>7</sup> F. Didierjean,<sup>15</sup> Y. Fang,<sup>10</sup> N. Fukuda,<sup>2</sup> G. Gey,<sup>16,17</sup> E. Ideguchi,<sup>10</sup> N. Inabe,<sup>2</sup> T. Isobe,<sup>2</sup> D. Kameda,<sup>2</sup> I. Kojouharov,<sup>18</sup> N. Kurz,<sup>18</sup> T. Kubo,<sup>2</sup> S. Lalkovski,<sup>19</sup> Z. Li,<sup>12</sup> R. Lozeva,<sup>15,20</sup> H. Nishibata,<sup>10</sup> A. Odahara,<sup>10</sup> Zs. Podolyák,<sup>7</sup> P. H. Regan,<sup>7,8</sup> O. J. Roberts,<sup>4</sup> H. Sakurai,<sup>2</sup> H. Schaffner,<sup>18</sup> G. S. Simpson,<sup>16</sup> H. Suzuki,<sup>2</sup> H. Takeda,<sup>2</sup> M. Tanaka,<sup>10,21</sup> J. Taprogge,<sup>2,22,23</sup> V. Werner,<sup>24,25</sup> and O. Wieland<sup>26</sup>

<sup>1</sup>Department of Physics and Astronomy, Seoul National University, Seoul 08826, Republic of Korea

<sup>2</sup>RIKEN Nishina Center, 2-1 Hirosawa, Wako-shi, Saitama 351-0198, Japan

<sup>3</sup>Department of Physics, Tohoku University, Aoba, Sendai, Miyagi 980-8578, Japan

<sup>4</sup>School of Computing, Engineering and Mathematics,

University of Brighton, Brighton BN2 4GJ, United Kingdom

<sup>5</sup>Center for Computational Sciences, University of Tsukuba, Tsukuba, 305-8577, Japan

<sup>6</sup>Faculty of Pure and Applied Sciences, University of Tsukuba, Tsukuba 305-8571, Japan

<sup>7</sup>Department of Physics, University of Surrey, Guildford GU2 7XH, United Kingdom

<sup>8</sup>National Physical Laboratory, Teddington, Middlesex, TW11 0LW, United Kingdom

<sup>9</sup>IRCNPC, School of Physics and Nuclear Energy Engineering, Beihang University, Beijing 100191, China

<sup>10</sup>Department of Physics, Osaka University, Toyonaka, Osaka 560-0043, Japan

<sup>11</sup>Department of Physics, University of York, Heslington, York YO10 5DD, United Kingdom

<sup>12</sup>Department of Physics, Peking University, Beijing 100871, China

<sup>13</sup>Department of Physics, University of Tokyo, Hongo, Bunkyo-ku, Tokyo 113-0033, Japan

<sup>14</sup>Department of Physics, University of Hong Kong, Pokfulam Road, Hong Kong

<sup>15</sup>IPHC, CNRS/IN2P3, Université de Strasbourg, 67037 Strasbourg, France

<sup>16</sup>LPSC, Université Grenoble-Alpes, CNRS/IN2P3, F-38026 Grenoble Cedex, France

<sup>17</sup>ILL, 38042 Grenoble Cedex, France

<sup>18</sup>GSI Helmholtzzentrum für Schwerionenforschung GmbH, 64291 Darmstadt, Germany

<sup>19</sup>Department of Physics, University of Sofia, 1164 Sofia, Bulgaria

<sup>20</sup>CSNSM, CNRS/IN2P3, Université Paris-Sud, F-91405 Orsay Campus, France

<sup>21</sup>Research Center for Nuclear Physics (RCNP), Osaka University, Ibaraki, Osaka 567-0047, Japan

<sup>22</sup>Departamento de Física Teórica, Universidad Autónoma de Madrid, E-28049 Madrid, Spain

<sup>23</sup>Instituto de Estructura de la Materia, CSIC, E-28006 Madrid, Spain

<sup>24</sup>A.W. Wright Nuclear Structure Laboratory, Yale University, New Haven, CT 06520, USA

<sup>25</sup>Institut für Kernphysik, Technische Universität Darmstadt, 64289 Darmstadt, Germany

<sup>26</sup>INFN Sezione di Milano, I-20133 Milano, Italy

(Dated: January 28, 2020)

The structure of  $^{106}\text{Mo}$ ,  $^{108}\text{Mo}$ , and  $^{110}\text{Mo}$  was investigated through  $\beta$ -delayed  $\gamma$ -ray spectroscopy at the RIKEN RI Beam Factory. New  $\gamma$ -ray transitions and levels are reported, including newly assigned  $0_2^+$  states in  $^{108,110}\text{Mo}$ . The  $\beta$ -delayed neutron-emission probabilities of  $^{108}\text{Nb}$  and  $^{110}\text{Nb}$  were determined by examining the  $\gamma$  rays of their respective daughter decays. Quadrupole deformations were obtained for  $^{106,108,110}\text{Mo}$  from their  $2_1^+$  energies and lifetimes. The even-odd energy staggering in the  $2_2^+$  band was compared with typical patterns of the  $\gamma$ -vibrational band, rigid triaxial rotor, and  $\gamma$ -soft rotor. The very small even-odd staggering of  $^{106}\text{Mo}$ ,  $^{108}\text{Mo}$ , and  $^{110}\text{Mo}$  favors a  $\gamma$ -vibrational band assignment. The kinematic moment of inertia for the  $2_2^+$  band showed a trend similar to the ground-state band, which is expected for the  $\gamma$ -vibrational band. Beyond-mean-field calculations employing the constrained Hartree-Fock-Bogoliubov (HFB) + local quasiparticle-random-phase approximation (QRPA) method using the SLy5+T interaction reproduced the ground and  $2_2^+$  bands in  $^{106}\text{Mo}$  and  $^{108}\text{Mo}$ . The collective wave functions are consistent with the interpretation of the  $2_2^+$  band as the  $\gamma$ -vibrational band of the prolate shape. However, the staggering pattern observed in  $^{110}\text{Mo}$  differs from the one suggested in the calculations which predict a  $\gamma$ -soft rotor. There was no experimental indication of the oblate shape or the  $\gamma$ -soft rotor predicted in heavier Mo isotopes.

## I. INTRODUCTION

The triaxial degree of freedom,  $\gamma$ , plays an important role in collective excitations of deformed even-even nuclei. While the first  $J^\pi = 2^+$  state ( $2_1^+$ ) is sensitive primarily to the quadrupole deformation parameter,  $\beta$ , the so-called  $\gamma$  band with a  $2^+$  band head is strongly related

\* hjs0314@snu.ac.kr

† sumikama@ribf.riken.jp

to triaxial motion [1]. In the case of axially-symmetric quadrupole deformation, a rotational band built on a  $\gamma$ -vibrational state constitutes the  $\gamma$  band. The energy of its band head is related to the softness of the vibrational motion in the  $\gamma$  direction. When the potential energy surface (PES) has a deep minimum between  $\gamma = 0^\circ$  (prolate) and  $60^\circ$  (oblate), the nucleus takes on a static triaxial shape and rotates about all three axes of the intrinsic body. The rigid triaxial rotor model by Davydov *et al.* [2] predicts that the  $2_2^+$  state lies below the  $4_1^+$  state at the maximum triaxiality of  $\gamma = 30^\circ$ . Another model of the triaxial shape is the  $\gamma$ -unstable rotor by Wilets and Jean [3], where PES has a  $\gamma$ -independent valley at a given  $\beta$ . The  $\gamma$ -unstable model predicts degenerate  $2_2^+$  and  $4_1^+$  states. A transitional rotor between the  $\gamma$ -vibrational band and the  $\gamma$ -unstable rotor is the  $\gamma$ -soft rotor, of which the PES has a moderate path between prolate and oblate [4].

The neutron-rich Mo isotopes are good candidates to investigate shape evolution in the  $\gamma$  degree of freedom. Calculations using the liquid-drop or the finite-range liquid-drop model using particle number projection or Bardeen-Cooper-Schrieffer methods predict the coexistence of prolate and oblate shapes, a prolate-to-oblate shape transition at  $N = 68$  or  $70$ , and triaxial ground states in  $^{104}\text{Mo}$ ,  $^{106}\text{Mo}$ , and  $^{108}\text{Mo}$  [5]. Hartree-Fock-Bogoliubov (HFB) calculations with the D1S-Gogny interaction [6] predict a gradual transition from  $\gamma$ -soft rotor in  $^{102}\text{Mo}$  to oblate in  $^{112}\text{Mo}$ . A calculation using the global Skyrme energy density functional UNEDF0 predicts triaxial ground-state deformation in  $^{106,108}\text{Mo}$  [7]. Calculations of two quasi-particle states are used to investigate quasi-particle configurations near the proton and neutron Fermi surfaces [8].

From the lifetime measurement of the ground-state band in  $^{100-108}\text{Mo}$  [9], the quadrupole deformation was indicated to reach a maximum at  $^{106}\text{Mo}$ . More precise measurements are awaited to obtain a certain conclusion, since uncertainties of transitional quadrupole moments are larger than a change among isotopes. The measured  $2_2^+$ -state energy,  $E(2_2^+)$ , in the neutron-rich Mo isotopes decreases as mass number,  $A$ , increases. It becomes almost equal to  $E(4_1^+)$  at  $A = 108$  and drops below  $E(4_1^+)$  at  $A \geq 110$  [10–16]. The low-lying  $2_2^+$  state in the neutron-rich Mo isotopes has been interpreted in terms of the rigid triaxial shape [12],  $\gamma$  vibration [13, 14], and  $\gamma$ -soft rotor [15] based on the measured values of the energies of the  $2_1^+$ ,  $4_1^+$ , and  $2_2^+$  states and the  $\gamma$ -decay branching ratio from  $2_2^+$  state. The interpretation of the  $2_2^+$  state attracts controversy due to its similarity between the three models, since the  $\gamma$ -vibrational state and  $\gamma$ -soft rotor have a finite root-mean-square value of  $\gamma$  as a result of a dynamic motion.

The energy staggering of the  $2_2^+$  band is a good signature to distinguish among the three models which describe axial asymmetry [1, 17]. The rigid-triaxial and  $\gamma$ -soft rotors show an energy staggering which deviates from the  $J(J+1)$  dependence of the rigid axial rotor.

The staggering of the rigid triaxial rotor is opposite to that of the  $\gamma$ -soft rotor; for example, the  $3_\gamma^+$  state is close to the  $2_\gamma^+$  and  $4_\gamma^+$  states of the rigid triaxial and  $\gamma$ -soft rotors, respectively, where the  $\gamma$  subscript indicates the band member of the  $2_2^+$  state. On the other hand, the  $\gamma$ -vibrational band with a small  $\gamma$  oscillation has a small or negligible staggering since the shape is close to being axially symmetric.

Another signature of  $\gamma$  vibration is the existence of a two-phonon  $\gamma$ -vibrational band based on the  $K = 4^+$  state. The  $K = 4^+$  band lying below the pairing gap was identified in the  $^{104,106,108}\text{Mo}$  isotopes with an energy ratio  $E_{K=4}/E_{K=2} = 1.95, 2.02$ , and  $2.42$  for  $^{104}\text{Mo}$ ,  $^{106}\text{Mo}$ , and  $^{108}\text{Mo}$ , respectively, which are close to the harmonic-vibrator value of 2 [13, 14].

The second  $0^+$  state provides additional information on the nuclear shape, since its origin can derive from  $\beta$  vibration or a coexisting shape. The  $0_2^+$  states in the neutron-rich Mo isotopes are assigned up to  $A = 106$  from  $\beta$  decay and (t,p) reaction studies [12, 18–20].

In the present study, the  $\beta$ -delayed  $\gamma$  rays of  $^{106,108,110}\text{Mo}$  were observed under lower background conditions and/or with higher statistics than the previous investigations [12, 15, 19, 21]. The lifetimes of the  $2_1^+$  states were measured using a fast timing array of 18  $\text{LaBr}_3(\text{Ce})$  crystals, of which preliminary results are reported in Ref. [22]. Reliable branching ratios of the  $2_2^+$  states were determined. The  $2_2^+$  band in  $^{110}\text{Mo}$  was extended from  $5^+$  to  $7^+$ . In  $^{108}\text{Mo}$  and  $^{110}\text{Mo}$ ,  $0_2^+$  states are newly assigned. It is observed that the previous  $0_2^+$  assignment in  $^{106}\text{Mo}$  [12] was incorrect. Values of quadrupole deformation and evidence for triaxial motion have been extracted from these measurements. The results are compared with beyond-mean-field calculations based on the five-dimensional collective Hamiltonian using the constrained HFB (CHFB) + local quasiparticle-random-phase approximation (LQRPA) approach.

## II. EXPERIMENT

The experiment was performed at RI Beam Factory (RIBF), operated by RIKEN Nishina Center and CNS, University of Tokyo. The RI beam was produced by the in-flight fission reaction of a  $345 \text{ MeV/u } ^{238}\text{U}^{86+}$  beam impinging on a 3.0-mm thick beryllium target. The RI beam was separated by the BigRIPS fragment separator and transported through the ZeroDegree spectrometer [23, 24]. The particle identification (PID) was performed by determining the mass-to-charge ratio,  $A/Q$ , and the atomic number,  $Z$  [25].

The RI beam was implanted into the active stopper WAS3ABi (Wide-range Active Silicon Strip Stopper Array for Beta and ion implantation), which comprised five stacked Double-Sided Silicon Strip Detectors (DSSSDs) [26]. The RI hit position of one DSSSD was determined by selecting the fastest timing signal of x and y strips [27]. The implanted layer was determined by de-

TABLE I. The number of  $^{106,108,110}\text{Zr}$  and  $^{106,108,110}\text{Nb}$  ions implanted in WAS3ABi and their implantation rate.

Isotope	The number of implanted ions	Implantation rate (pps)
$^{106}\text{Zr}$	$1.9 \times 10^6$	3.5
$^{108}\text{Zr}$	$2.1 \times 10^6$	3.8
$^{110}\text{Zr}$	$3.2 \times 10^4$	0.059
$^{106}\text{Nb}$	$7.1 \times 10^4$	16
$^{108}\text{Nb}$	$1.3 \times 10^5$	0.24
$^{110}\text{Nb}$	$1.9 \times 10^6$	3.5

detecting the cross-talk signal induced to the DSSSD downstream of the implanted one [28].

The  $\beta$  particles emitted by the decay of the RI were measured by WAS3ABi and two plastic scintillators with 2 mm thickness, placed upstream and downstream of WAS3ABi. The timing signal of the plastic scintillator was used for the high-time resolution detection of  $\beta$  particles. The  $\beta$ -particle hit pattern and energy deposition in WAS3ABi and the plastic scintillators were used to restrict position candidates of the  $\beta$  emitter [29]. The  $\beta$  particle was associated with the implanted RI by using the position and time differences between the RI and  $\beta$  particle.

WAS3ABi was surrounded by the EUROball-RIKEN Cluster Array (EURICA) [30] to detect  $\gamma$  rays emitted from excited states populated by the  $\beta$  decay of implanted RIs. The systematic uncertainty of  $\gamma$ -ray energy was evaluated to be 0.15 keV from the residuals of the energy calibration with standard  $\gamma$ -ray sources. The  $\gamma$ -ray detection efficiency of EURICA was measured to be 18.3% at 250 keV and 8.1% at 1 MeV. A systematic uncertainty of 5% was determined for the absolute value from the uncertainty of the radioactivity of the  $\gamma$ -ray sources. A fast-timing  $\text{LaBr}_3(\text{Ce})$  array consisting of eighteen  $\phi 1.5'' \times 2''$  crystals was coupled to the EURICA array to measure the lifetimes of low-lying excited states in the nanosecond regime [31]. The Full-Width Half Maximum (FWHM) of the time resolution of the  $\text{LaBr}_3(\text{Ce})$  array was evaluated to be 0.61 ns at 200 keV. The  $\gamma$ -ray detection efficiency was 3.0(5)% and 0.7(2)% at 250 keV and 1 MeV, respectively.

Excited states in  $^{106,108,110}\text{Mo}$  populated in the beta decay of  $^{106,108,110}\text{Nb}$  were studied. The daughter decays of Zr isotopes were also analyzed to increase statistics and to search for  $\beta$ -decaying isomeric states. The number of implanted Nb and Zr isotopes are summarized in Table I. Daughter-decay analysis provides evidence on the existence of  $\beta$ -decaying isomeric states. For example, in Ref. [32], the  $\beta$ - $\gamma$  spectrum of  $^{102}\text{Zr}$  was observed through the  $\beta$  decay of  $^{102}\text{Y}$  and the  $\beta$ -decay chain of  $^{102}\text{Sr} \rightarrow ^{102}\text{Y} \rightarrow ^{102}\text{Zr}$ . Two different  $\gamma$ -ray transition patterns revealed that  $^{102}\text{Y}$  has a  $\beta$ -decaying isomeric state and the  $\beta$  decay of the even-even  $^{102}\text{Sr}$  isotope with the

spin-parity of  $0^+$  can only populate the  $\beta$ -decaying low spin state in  $^{102}\text{Y}$ . The same method was applied to the  $\text{Zr} \rightarrow \text{Nb} \rightarrow \text{Mo}$   $\beta$ -decay chain in this work. For each  $\beta$ -decay chain,  $\text{Zr} \rightarrow \text{Nb} \rightarrow \text{Mo}$  or  $\text{Nb} \rightarrow \text{Mo}$ , the  $\beta$ -ion time window was optimized to maximize the number of the Nb-decay events and minimize the number of other decays.

### III. RESULTS

#### A. $\beta$ decay to $^{106}\text{Mo}$

The  $\beta$ -delayed  $\gamma$ -ray spectrum of  $^{106}\text{Mo}$  obtained from the  $\beta$ -decay chain  $^{106}\text{Zr} \rightarrow ^{106}\text{Nb} \rightarrow ^{106}\text{Mo}$  is shown in Figs. 1 (a–b). The proposed level scheme of  $^{106}\text{Mo}$ , illustrated in Fig. 2, was constructed through the use of  $\gamma$ -ray coincidences, for example Figs. 1 (c–d), energy sums and intensity balances. Nine new levels were identified and a new transition from the  $2_2^+$  to  $4_1^+$  states was observed. In the previous  $\beta$ - $\gamma$  spectroscopic study [12], the ground band was observed up to  $6^+$ , and the  $2_2^+$  and  $4_3^+$  bands up to  $4^+$ . In the present study,  $\gamma$  rays from the  $5^+$  states in the  $2_2^+$  and  $4_3^+$  bands were observed. These  $\gamma$  rays are consistent with the results obtained from the spontaneous fission of  $^{252}\text{Cf}$  [35–37]. The placement of the 784.6-keV and 1106.7-keV  $\gamma$  rays were reassigned from those of Ref. [12] based on the following arguments. The  $0_2^+$  state was previously assigned at 956.6 keV based on the 784.6-keV transition feeding only the 171.4-keV level. However, the high statistics of the present study allowed us to observe additional coincidences with the 784.6-keV transition, which are shown in Fig. 1 (d). Based on this information, the assignment of the 784.6-keV  $\gamma$  ray as the transition between the  $5_1^+$  and  $4_1^+$  states is preferred. The observation of the transition from  $5_1^+$  to  $3_1^+$  supports this assignment. The previous assignment of the 1106.7-keV  $\gamma$  ray was the transition between a 1279.9-keV state to the  $2_1^+$  state [12], but it was reassigned to a known transition [34] from the 1816.9-keV state, since a coincidence with 710.2 keV was observed. The half life of  $^{106}\text{Nb}$  was determined to be 1.10(5) s from the decay curve of the 171.4-keV  $\gamma$  ray for the  $^{106}\text{Nb} \rightarrow ^{106}\text{Mo}$  decay as shown in Fig. 3 (a). The obtained half life was consistent with the evaluated value of 1.02(5) s [34].

Table II summarizes the relative  $\gamma$ -ray intensity,  $I_\gamma$ , following the  $\beta$  decay from  $^{106}\text{Nb}$  to  $^{106}\text{Mo}$  from the two decay chains,  $^{106}\text{Nb} \rightarrow ^{106}\text{Mo}$  and  $^{106}\text{Zr} \rightarrow ^{106}\text{Nb} \rightarrow ^{106}\text{Mo}$ . Since  $I_\gamma$  of the major peaks was consistent between both decay chains, there was no evidence on the existence of a second  $\beta$ -decaying state in  $^{106}\text{Nb}$ . The absolute  $\gamma$ -ray intensities per 100  $\beta$  decays were determined from the data of the  $^{106}\text{Nb} \rightarrow ^{106}\text{Mo}$  decay for the first time. Here, we used the number of the detected  $\beta$  particles emitted from the  $^{106}\text{Nb}$  decay, which was determined from the decay-curve integral of the parent component in the fitting function to the  $\beta$ -particle counts as a function of time. The conversion factor from the relative to absolute  $\gamma$ -ray in-

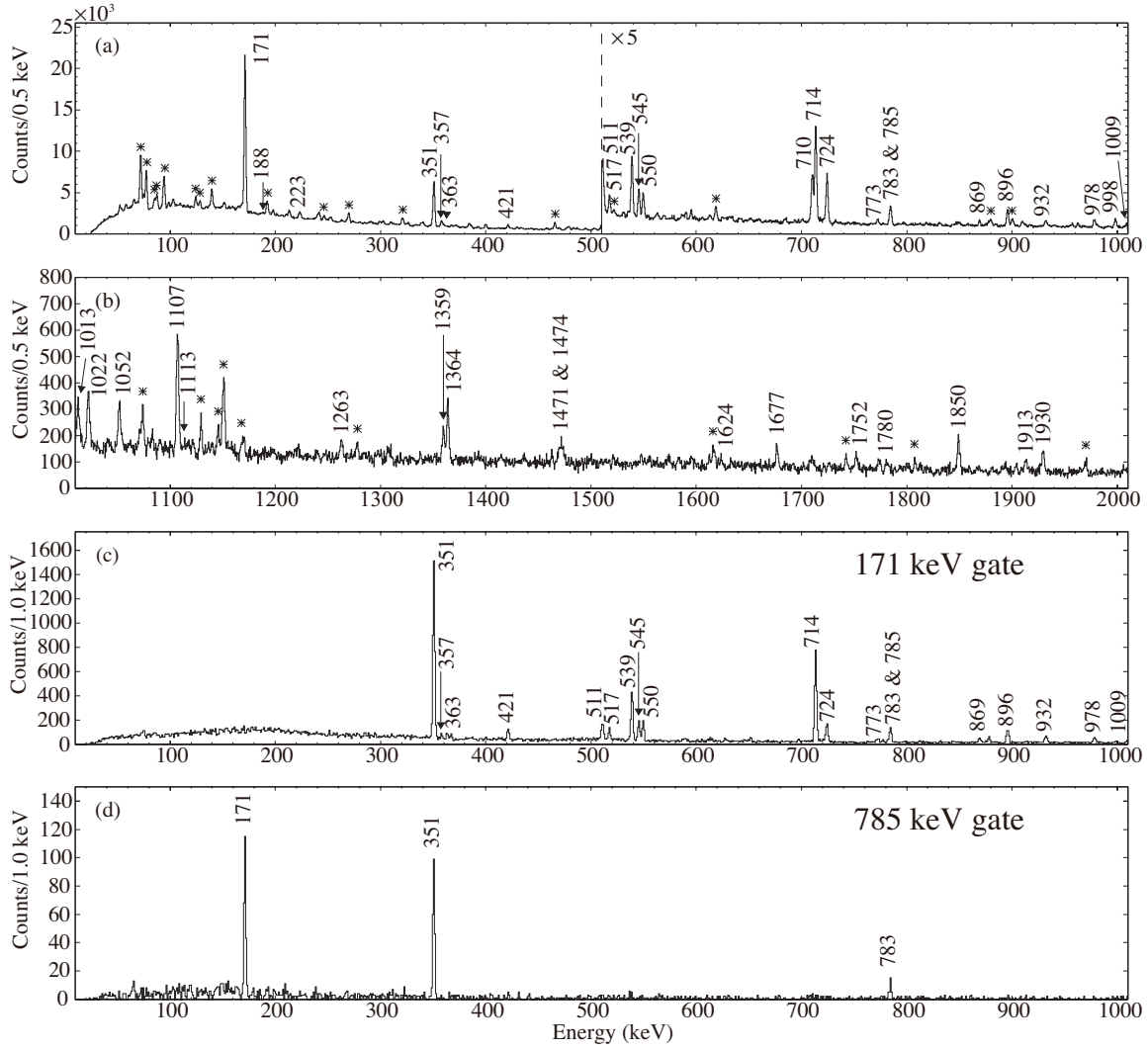


FIG. 1. (a–b) The  $\beta$ -delayed  $\gamma$ -ray spectrum of  $^{106}\text{Nb}$  obtained from the  $\beta$ -decay chain  $^{106}\text{Zr} \rightarrow ^{106}\text{Nb} \rightarrow ^{106}\text{Mo}$ . The range of the time window was set to be  $180 \text{ ms} < t_{\text{ion}} - t_{\beta} < 2200 \text{ ms}$ . The labeled peaks belong to  $^{106}\text{Mo}$ . The identified background peaks are marked with asterisks. Other unknown peaks are mainly associated with parent  $^{106}\text{Zr}$  decays. (c–d) The coincidence spectra gated on 171.4 keV and 784.6 keV.

tensities was obtained from the absolute intensity of the largest  $\gamma$ -ray peak at 171.4 keV in the  $^{106}\text{Nb} \rightarrow ^{106}\text{Mo}$  decay. The relative systematic uncertainty of the absolute  $\gamma$ -ray detection efficiency was adopted into the uncertainty of the conversion factor as 0.696(38).

The  $\beta$ -decay intensities,  $I_{\beta}$ , to excited states, given in Table II, were determined by combining results obtained from the  $^{106}\text{Zr} \rightarrow ^{106}\text{Nb} \rightarrow ^{106}\text{Mo}$  and  $^{106}\text{Nb} \rightarrow ^{106}\text{Mo}$  decay chains so as to take into account small  $\beta$ -decay branches. The decay schemes and  $I_{\gamma}$  values were obtained from the  $^{106}\text{Zr} \rightarrow ^{106}\text{Nb} \rightarrow ^{106}\text{Mo}$  decay chain, which provided higher statistics. The total  $I_{\beta}$  of all  $\gamma$ -decaying excited states is given by summing the absolute transition intensities of excited states decaying to the ground state.

Two relevant transitions,  $2_1^+ \rightarrow 0_1^+$  and  $2_2^+ \rightarrow 0_1^+$ , were observed. The sum of the absolute intensities of these two transitions was 92.2(51)%, which included contributions of possible undetected transitions, due to low intensities, through the  $2_1^+$  or  $2_2^+$  states. The remaining 7.8(51)% contribution is the sum of  $I_{\beta}$  to the ground state, and the  $\beta$ -delayed neutron emission probability,  $P_n$ . When a previously measured  $P_n$  of 4.5(3)% [34] is subtracted, the  $I_{\beta}$  value to the ground state is given as the upper limit  $< 8.4\%$ .

Table II summarizes the  $\log ft$  value of each excited state calculated using  $Q(\beta^-) = 9931(10) \text{ keV}$  from the atomic mass evaluation (AME2016) [33] and the calculation tool of Ref. [38]. The  $\log ft$  of the  $6_1^+$  state, 6.6(1),

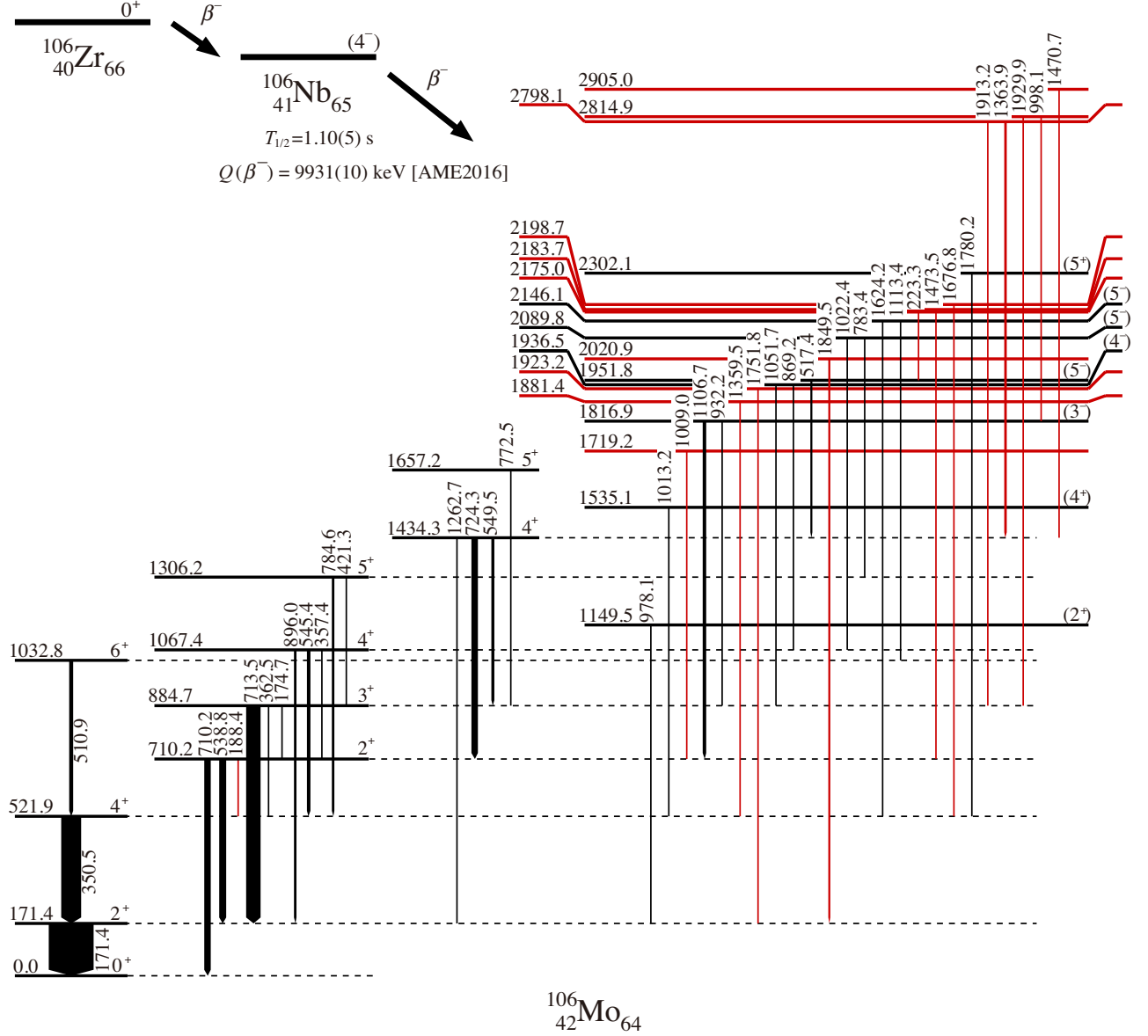


FIG. 2. The proposed level scheme of  $^{106}\text{Mo}$  obtained from the  $\beta$ -decay chain  $^{106}\text{Zr} \rightarrow ^{106}\text{Nb} \rightarrow ^{106}\text{Mo}$ . The  $Q(\beta^-)$  of  $^{106}\text{Nb}$  is taken from the atomic mass evaluation (AME2016: [33]). The arrow width is proportional to the relative intensity  $I_\gamma$  ( $\text{Zr} \rightarrow \text{Mo}$ , given in Table II). Red lines are the new levels and transitions. Spin-parities of the known states are taken from ENSDF [34].

TABLE II: The level energy,  $E_i$ , spin-parity,  $J^\pi$ ,  $\gamma$ -ray energy,  $E_\gamma$ , relative  $\gamma$ -ray intensity,  $I_\gamma$ ,  $\beta$ -decay intensity,  $I_\beta$ , and  $\log ft$  of the excited states in  $^{106}\text{Mo}$ . (Nb $\rightarrow$ Mo) indicates the  $\beta$  decay from the implanted  $^{106}\text{Nb}$  to  $^{106}\text{Mo}$ . (Zr $\rightarrow$ Mo) indicates the  $\beta$  decay to  $^{106}\text{Mo}$  in the decay chain of the implanted  $^{106}\text{Zr}$ , i.e.  $^{106}\text{Zr} \rightarrow ^{106}\text{Nb} \rightarrow ^{106}\text{Mo}$ . (allowed/non-UF) indicates the calculation is for the allowed or non-unique forbidden transitions. (1UF) is for the first unique forbidden transition from  $4^-$  to  $2^+$  or  $6^+$  states.

$E_i$ (keV)	$J^\pi$	$E_\gamma$ (keV)	$I_\gamma^a$ (Nb $\rightarrow$ Mo)	$I_\gamma$ (Zr $\rightarrow$ Mo)	$I_\beta(\%)^b$	$\log ft$ (allowed/non-UF)	$\log ft$ (1UF)
0.0	$0^+$				$< 8.4$		
171.4(2)	$2^+$	171.4(2)	100(2)	100.0(5)	7.3(8)	6.7(1)	9.1(1)
521.9(2)	$4^+$	350.5(2)	37.9(16)	43.8(5)	9.1(14)	6.5(1)	

TABLE II: (continued)

$E_i$ (keV)	$J^\pi$	$E_\gamma$ (keV)	$I_\gamma^a$ (Nb→Mo)	$I_\gamma$ (Zr→Mo)	$I_\beta(\%)^b$	$\log ft$ (allowed/non-UF)	$\log ft$ (1UF)
710.2(1)	2 <sup>+</sup>	188.4(4)	2.9(7)	0.3(2)	2.8(6)	7.0(1)	9.3(1)
		538.8(2)	16.6(12)	15.6(3)			
		710.2(2)	14.4(15)	15.2(3)			
884.7(2)	3 <sup>+</sup>	174.7(3)		1.0(4)	8.7(7)	6.5(1)	
		362.5(3)	1.7(7)	0.7(2)			
		713.5(2)	30.1(17)	31.9(4)			
1032.8(3)	6 <sup>+</sup>	510.9(2)	5.3(12)	8.2(15)	5.5(11)	6.6(1)	8.9(1)
1067.4(1)	4 <sup>+</sup>	357.4(2)	3.9(8)	2.1(2)	7.9(5)	6.5(1)	
		545.4(2)	5.3(10)	7.6(2)			
		896.0(2)	6.1(10)	6.1(2)			
1149.5(2)	(2 <sup>+</sup> )	978.1(2)		2.3(2)	1.6(2)	7.1(1)	9.4(1)
1306.2(2)	5 <sup>+</sup>	421.3(2)	3.1(7)	3.5(2)	5.4(8)	6.6(1)	
		784.6(2)	3.4(8)	5.5(7)			
1434.3(1)	4 <sup>+</sup>	549.5(2)	5.1(9)	6.9(2)	7.0(5)	6.4(1)	
		724.3(2)	11.7(12)	14.0(3)			
		1262.7(3)		1.4(2)			
1535.1(3)	(4 <sup>+</sup> )	1013.2(2)		1.5(3)	1.0(2)	7.2(1)	
1657.2(3)	5 <sup>+</sup>	772.5(2)		1.4(2)	1.0(1)	7.2(1)	
1719.2(2)		1009.0(2)		1.3(2)	0.9(1)	7.2(1)	
1816.9(2)	(3 <sup>-</sup> )	932.2(2)	1.3(7)	2.0(2)	4.9(4)	6.5(1)	
		1106.7(2)	4.0(8)	7.4(3)			
1881.4(3)		1359.5(2)		2.9(2)	2.0(2)	6.9(1)	
1923.2(2)		1751.8(2)		1.6(2)	1.1(2)	7.1(1)	
1936.5(2)	(4 <sup>-</sup> )	869.2(2)		2.0(2)	3.5(3)	6.6(1)	
		1051.7(2)	2.9(2)	3.1(2)			
1951.8(2)	(5 <sup>-</sup> )	517.4(2)	6.2(9)	4.6(2)	2.3(2)	6.8(1)	
2020.9(2)		1849.5(2)	3.2(14)	4.1(3)	2.9(3)	6.7(1)	
2089.8(2)	(5 <sup>-</sup> )	783.4(4)	2.6(11)	1.3(7)	2.7(5)	6.7(1)	
		1022.4(2)		2.5(2)			
2146.1(4)	(5 <sup>-</sup> )	1113.4(5)		0.3(2)	0.5(2)	7.4(2)	
		1624.2(4)		0.4(2)			
2175.0(3)		223.3(2)		1.3(2)	0.9(1)	7.1(1)	
2183.7(4)		1473.5(3)		1.3(2)	0.9(1)	7.1(1)	
2198.7(3)		1676.8(2)		2.2(2)	1.5(2)	6.9(1)	
2302.1(3)	(5 <sup>+</sup> )	1780.2(3)		1.4(2)	1.0(1)	7.1(1)	
2798.1(2)		1363.9(2)	6.3(9)	5.9(2)	5.2(3)	6.2(1)	
		1913.2(3)		1.5(1)			
2814.9(2)		998.1(2)		2.3(1)	3.5(2)	6.4(1)	
		1929.9(2)		2.7(2)			
2905.0(3)		1470.7(3)		1.7(2)	1.2(2)	6.8(1)	

<sup>a</sup> The absolute intensity per 100  $\beta$ -decays is 0.696(38) $I_\gamma$ .<sup>b</sup> Internal conversion coefficients, calculated using the BrIcc code [39], were adopted for three transitions with 171.4, 174.7, and 188.4 keV.

indicates an allowed transition with  $\Delta J = 0$  or 1 and  $\Delta\pi = 0$ , or a first non-unique forbidden transition with  $\Delta J = 0$  or 1 and  $\Delta\pi = 1$  [40]. Three 2<sup>+</sup> states have similar  $\log ft$  values ranging from 6.7 to 7.1 which also indicates allowed or first non-unique forbidden transitions. However, the transitions with  $\Delta J \leq 1$  can not populate both the 2<sup>+</sup> and 6<sup>+</sup> states. Therefore, transitions with at least  $\Delta J = 2$  are required for these states. For the

unique forbidden transitions, the  $\log ft$  values need to be calculated by taking into account the different energy dependence of the shape factor from that of the allowed decay [38, 41]. The  $\log ft$  of the  $6_1^+$  state becomes 8.9(1) for the first unique forbidden transition with  $\Delta J = 2$  and  $\Delta\pi = 1$ . This value is consistent with the typical range from 8 to 11 [40]. This indicates that the spin-parity of  $^{106}\text{Nb}$  is  $4^-$ . This assignment determines the transition type to other states. Since the  $\beta$  decay to the  $2^+$  states is also a first unique forbidden transition, the  $\log ft$  values of the  $2^+$  states with 171.4, 710.2, and 1149.5 keV were recalculated as 9.1(1), 8.9(1), and 9.4(1), respectively. These values are consistent with the typical range of the first unique forbidden transition. The  $\log ft$  values of the  $3^-$ ,  $4^-$ , and  $5^-$  states are consistent with the allowed transition with  $\Delta J = 0$  or 1 and  $\Delta\pi = 0$ , and those of  $3^+$ ,  $4^+$ , and  $5^+$  states are consistent with the first non-unique forbidden transition with  $\Delta J = 0$  or 1 and  $\Delta\pi = 1$ . Thus, providing further evidence that the spin-parity of  $^{106}\text{Nb}$  is  $4^-$ . The quasi-particle state configuration of  $^{106}\text{Nb}$  is discussed in Sec. IV F.

### B. $\beta$ decay to $^{108}\text{Mo}$

The  $\beta$ -delayed  $\gamma$ -ray spectrum of  $^{108}\text{Mo}$  obtained from the  $^{108}\text{Zr} \rightarrow ^{108}\text{Nb} \rightarrow ^{108}\text{Mo}$  decay chain is shown in Figs. 4 (a–b). The proposed level scheme illustrated in Fig. 5 was constructed through the use of  $\gamma$ -ray coincidences, examples shown in Figs. 4 (c–d), energy sums, and intensity balances. In the previous  $\beta$ -decay study [21], the ground band was observed up to  $4^+$  and the  $2_2^+$  band was up to  $3^+$ . In this work, the  $2_2^+$  band was observed up to  $4^+$ , and the band head of the  $4^+$  band was observed at 1422.1 keV. Fifteen new levels were identified, of which the lowest at 893.4 keV was assigned to  $0_2^+$  from the typical  $\gamma$  decay pattern of a low-lying  $0^+$  state, namely the observed 700.7-keV transition was measured to be in strong coincidence with the  $2_1^+ \rightarrow 0_1^+$  transition, as shown in Fig. 4 (c), and without an observed  $\gamma$  decay to the  $0_1^+$  state. The spin-parity of the 1158.4-keV state was assigned to be  $2^+$ , and those of the 1404.8-, and 1727.6-keV states were to be  $3$  or  $4^+$  by assuming the transition type from those states is E1 or M1/E2. The half life of the  $^{108}\text{Nb}$  decay was determined to be  $T_{1/2} = 186(8)$  ms from the decay curve of the 192.8-keV  $\gamma$  ray, as shown in Fig. 3 (b), and is consistent with the evaluated value of 198(6) ms [34].

The  $I_\gamma$  values were determined for the two decay chains,  $^{108}\text{Nb} \rightarrow ^{108}\text{Mo}$  and  $^{108}\text{Zr} \rightarrow ^{108}\text{Nb} \rightarrow ^{108}\text{Mo}$ , as summarized in Table III. The consistent  $I_\gamma$  values between two decay chains indicate no  $\beta$ -decaying isomeric state in  $^{108}\text{Nb}$ . The conversion factor from the relative to absolute  $\gamma$ -ray intensities was determined from the absolute 192.8-keV intensity in the  $^{108}\text{Nb} \rightarrow ^{108}\text{Mo}$  decay.

The  $I_\beta$  values were determined from the absolute intensities and the decay scheme. As described in Sec. III A, the total  $I_\beta$  of the  $\gamma$ -decaying excited states in  $^{108}\text{Mo}$

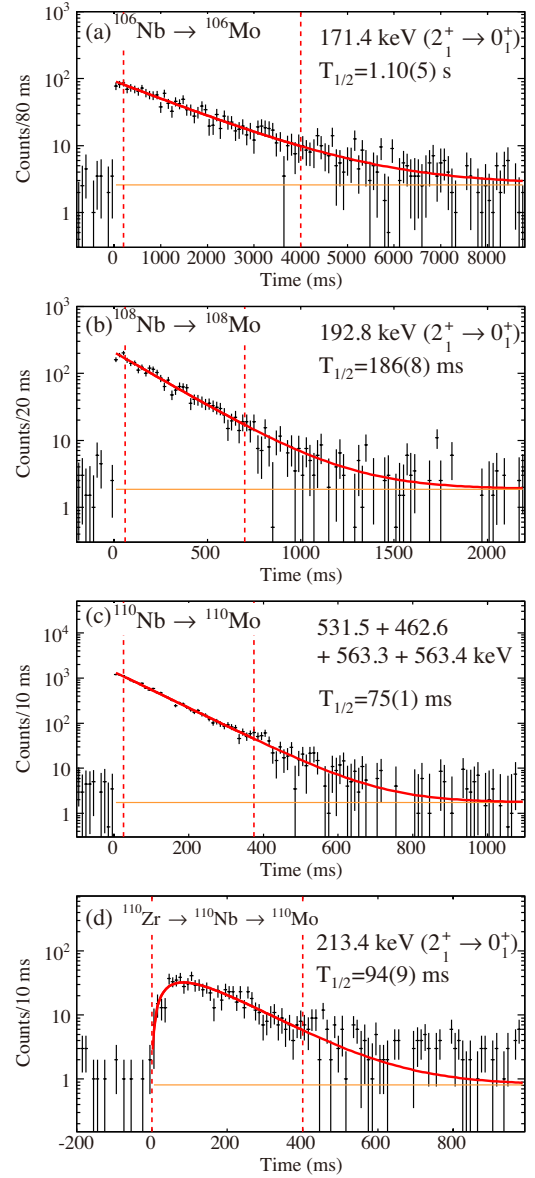


FIG. 3. The time spectra of  $\beta$ -delayed  $\gamma$  rays in the Mo isotopes. Dashed lines indicate the fitting region of the decay curve to determine the  $\beta$ -decay half life,  $T_{1/2}$ . Orange lines are the constant background, which was determined by fitting to the negative-time region. The  $\beta$ -delayed  $\gamma$  rays with 531.5, 462.6, 563.3, and 563.4 keV from the implanted  $^{110}\text{Nb}$  were selected as the  $\beta$  decays of the high-spin state in  $^{110}\text{Nb}$ .

was determined to be 62.8(33)% from the sum of absolute transition intensities of three transitions from the  $2_1^+$ ,  $2_2^+$ , and  $2_3^+$  states to the ground state. The zero-neutron emission probability of the  $^{108}\text{Nb}$  decay,  $P_{0n}$ , which is the probability decaying to  $^{108}\text{Mo}$  without a delayed-neutron emission, was determined by using a new method described in Sec. III C as,  $P_{0n} = 82(11)\%$ . The difference of these two values gave the ground-state  $I_\beta$  of 19(12)%. The  $I_\gamma$  values obtained in this work are inconsistent with the previous results [21] with the exception of the



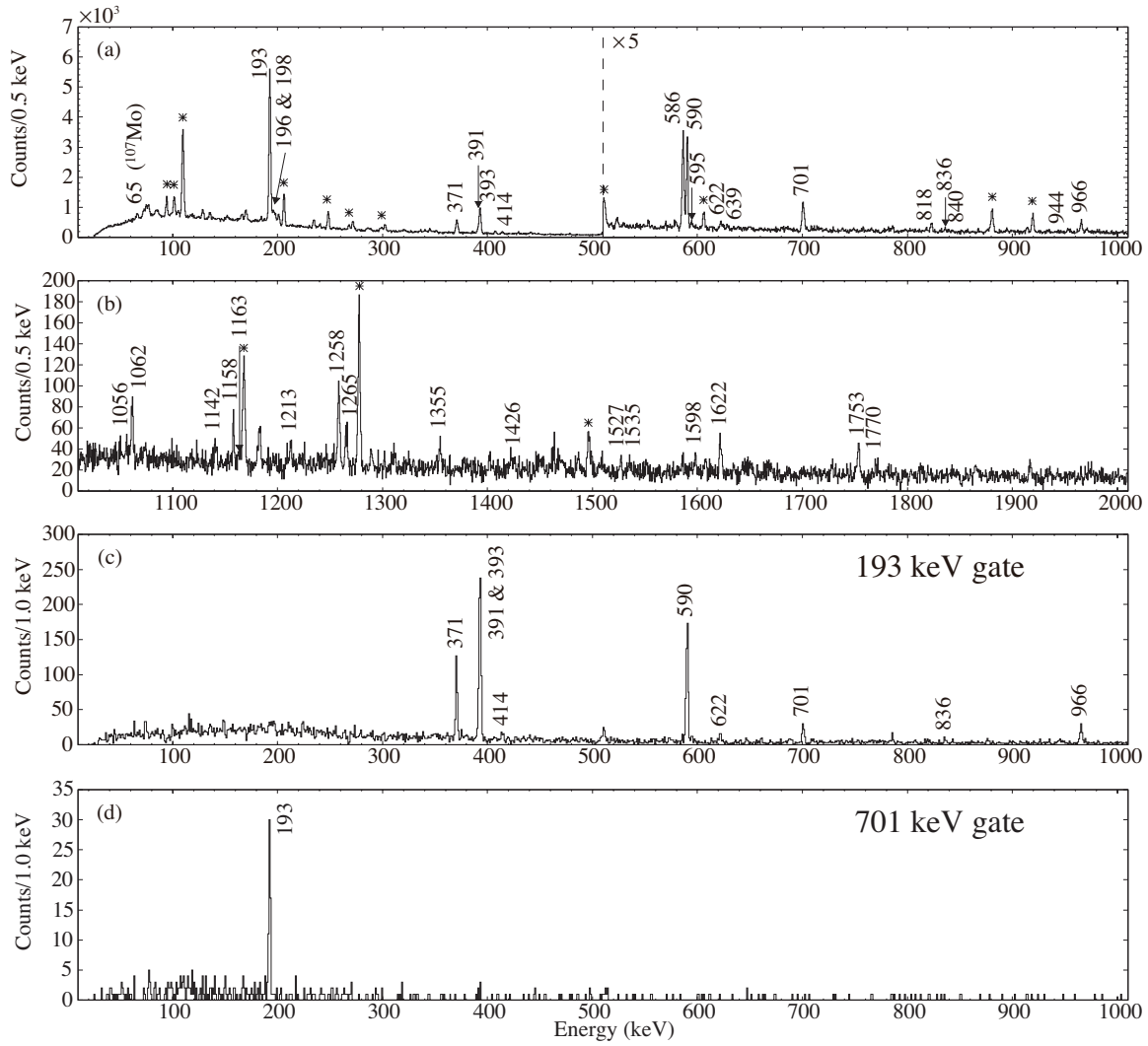


FIG. 4. (a–b) The  $\beta$ -delayed  $\gamma$ -ray spectrum of  $^{108}\text{Nb}$  obtained from the  $\beta$ -decay chain  $^{108}\text{Zr} \rightarrow ^{108}\text{Nb} \rightarrow ^{108}\text{Mo}$ . The range of the time window was set to be  $80 \text{ ms} < t_{\text{ion}} - t_{\beta} < 280 \text{ ms}$ . The labeled peaks belong to  $^{108}\text{Mo}$ . The identified background peaks are marked with asterisks. Other unknown peaks are mainly associated with parent  $^{108}\text{Zr}$  decays. (c–d) The coincidence spectra gated on 192.8 keV and 700.7 keV.

371.1- and 393.1-keV  $\gamma$  rays. Notably the  $I_{\gamma}(590.1 \text{ keV})$  of 26.1(6)% was roughly half of that reported in Ref. [21], 53%. As mentioned in Ref. [21], a large background in their  $\gamma$ -ray spectrum might be the cause of the inconsistency. The absolute intensity of the  $2_1^+ \rightarrow 0_1^+$  transition was also roughly half of that reported in Ref. [21]. This may be due to a 50% uncertainty of the  $^{108}\text{Nb}$  yield extrapolated as a function of the atomic number [21]. Although the uncertainty of the previous  $I_{\beta}$  was not evaluated, the present  $I_{\beta}(3_1^+)$  of 5.1(6)% is 1/10 of the reported 53% [21] owing to yield uncertainties and the previous non-observation of the cascade transitions to the  $3_1^+$  state.

The  $\log ft$  values were determined from  $T_{1/2}$ ,  $I_{\beta}$ , and  $Q_{\beta} = 11210(12) \text{ keV}$  [33]. The  $\log ft$  values of the  $0_1^+$

and  $4_1^+$  states were 5.8(3) and 6.4(1) and are too small for any transitions with  $\Delta J \geq 2$  [40]. This is the same situation as for the  $^{106}\text{Nb}$  decay. If the first unique forbidden transition with  $\Delta J = 2$  and  $\Delta\pi = 1$  is considered for the transitions to these states, the spin-parity of the  $^{108}\text{Nb}$  ground state is  $2^-$ . The  $\log ft$  values of the  $0^+$  and  $4^+$  states were recalculated as the first unique forbidden transition to be 8.2(3), 8.8(1), 8.7(1), 8.5(1), and 9.2(1) for the ground state and the excited states at 563.8 keV, 893.4 keV, 978.3 keV, and 1422.1 keV, respectively. These are within the typical range from 8 to 11 [40]. The  $\log ft$  values of the  $2^+$ ,  $3^+$ , and  $3^-$  states indicate the allowed transition or the first non-unique forbidden transition, and are consistent with the  $\beta$  decay from a  $2^-$  state. The  $\beta$  decay to the  $5^-$  state at 2161.8 keV is the

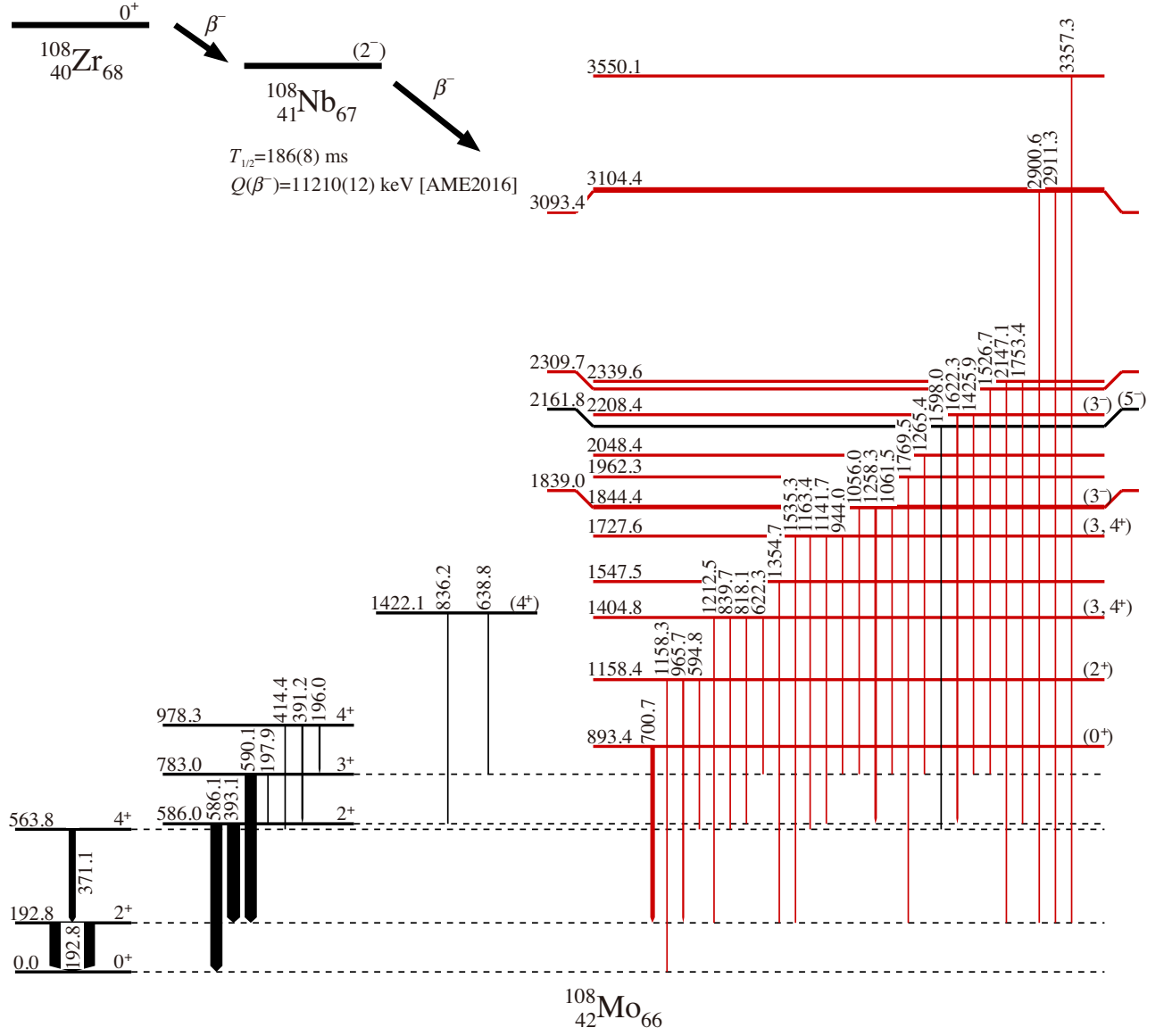


FIG. 5. The proposed level scheme of  $^{108}\text{Mo}$  obtained from the  $\beta$ -decay chain  $^{108}\text{Zr} \rightarrow ^{108}\text{Nb} \rightarrow ^{108}\text{Mo}$ . Red lines are the new levels and transitions.

TABLE III: Same as Table II, but for  $^{108}\text{Mo}$ . (1UF) is for the first unique forbidden transition from  $2^-$  to  $0^+$  or  $4^+$  states. (2UF) is for the second unique forbidden transition from  $2^-$  to  $5^-$  states.

$E_i$ (keV)	$J^\pi$	$E_\gamma$ (keV)	$I_\gamma^a$ (Nb $\rightarrow$ Mo)	$I_\gamma$ (Zr $\rightarrow$ Mo)	$I_\beta(\%)^b$	logft (allowed/non-UF)	logft (1UF)	logft (2UF)
0.0	$0^+$				19(12)	5.8(3)	8.2(3)	
192.8(2)	$2^+$	192.8(2)	100(2)	100.0(9)	6.7(10)	6.2(1)		
563.8(2)	$4^+$	371.1(2)	18.2(10)	14.5(5)	3.7(6)	6.4(1)	8.8(1)	
586.0(1)	$2^+$	393.1(2)	28.3(13)	27.8(10)	13.2(12)	5.8(1)		
		586.1(2)	25.0(12)	26.4(7)				
783.0(2)	$3^+$	197.9(6)		3.4(1)	5.1(6)	6.2(1)		
		590.1(2)	27.4(12)	26.1(6)				
893.4(2)	$(0^+)$	700.7(2)	4.7(16)	9.7(5)	4.3(3)	6.3(1)	8.7(1)	

TABLE III: (continued)

$E_i$ (keV)	$J^\pi$	$E_\gamma$ (keV)	$I_\gamma^a$ (Nb→Mo)	$I_\gamma$ (Zr→Mo)	$I_\beta(\%)^b$	log $ft$ (allowed/non-UF)	log $ft$ (1UF)	log $ft$ (2UF)
978.3(2)	4 <sup>+</sup>	196.0(2)		5.0(1)	5.4(7)	6.1(1)	8.5(1)	
		391.2(3)	7.0(9)	4.5(14)				
		414.4(3)	2.1(5)	2.3(6)				
1158.4(1)	(2 <sup>+</sup> )	594.8(3)	1.2(5)	1.5(4)	3.8(4)	6.3(1)		
		965.7(2)	4.2(7)	4.4(4)				
		1158.3(2)	3.2(6)	2.5(4)				
1404.8(2)	(3, 4 <sup>+</sup> )	622.3(3)		1.7(4)	2.1(3)	6.5(1)		
		818.1(4)		0.8(3)				
		839.7(3)		0.7(3)				
		1212.5(3)		1.4(4)				
1422.1(2)	(4 <sup>+</sup> )	638.8(4)	0.6(1)	0.5(3)	0.9(2)	6.8(1)	9.2(1)	
		836.2(3)		1.4(3)				
1547.5(3)		1354.7(2)		2.1(4)	0.9(2)	6.8(1)		
1727.6(2)	(3, 4 <sup>+</sup> )	944.0(5)		0.4(3)	1.5(3)	6.5(1)		
		1141.7(3)		1.4(3)				
		1163.4(6)		0.5(5)				
		1535.3(4)		1.1(3)				
1839.0(5)		1056.0(4)		0.8(3)	0.4(1)	7.1(1)		
1844.4(2)	(3 <sup>-</sup> )	1061.5(2)	2.2(1)	3.6(4)	4.1(4)	6.1(1)		
		1258.3(2)	7.5(6)	5.6(5)				
1962.3(2)		1769.5(2)		0.8(1)	0.4(1)	7.1(1)		
2048.4(3)		1265.4(2)	3.3(5)	3.1(4)	1.4(2)	6.5(1)		
2161.8(4)	(5 <sup>-</sup> )	1598.0(3)		1.2(5)	0.5(2)	6.9(2)		11.6(2)
2208.4(2)	(3 <sup>-</sup> )	1425.9(7)		1.1(3)	2.4(3)	6.2(1)		
		1622.3(2)		4.2(4)				
2309.7(3)		1526.7(3)		1.8(3)	0.8(1)	6.7(1)		
2339.6(2)		1753.4(3)		3.3(5)	2.8(3)	6.1(1)		
		2147.1(3)		3.0(4)				
3093.4(5)		2900.6(4)		1.6(4)	0.7(2)	6.6(1)		
3104.1(4)		2911.3(3)		2.3(5)	1.0(2)	6.4(1)		
3550.1(5)		3357.3(4)		1.6(6)	0.7(3)	6.4(2)		

<sup>a</sup> The absolute intensity per 100  $\beta$ -decays is 0.448(23) $I_\gamma$ .

<sup>b</sup> Internal conversion coefficients, calculated using the BrIcc code [39], were adopted for three transitions with 192.8, 196.0, and 197.9 keV.

second unique forbidden transition with  $\Delta J = 3$  and  $\Delta\pi = 0$ . The log  $ft$  value of the 5<sup>-</sup> state was recalculated to be 11.6(2) and within the typical range from 10.6 to 18 for the second unique forbidden transition [40]. Therefore, the spin-parity of the <sup>108</sup>Nb was assigned to be 2<sup>-</sup>. The quasi-particle state configuration of <sup>108</sup>Nb is described in Sec. IV F.

### C. Neutron-emission probability in <sup>108</sup>Nb $\beta$ decay

The zero-neutron emission probability,  $P_{0n}$ , of the <sup>108</sup>Nb decay is given by the ratio  $N_\beta(^{108}\text{Mo})/N_\beta(^{108}\text{Nb})$ , where  $N_\beta(^{108}\text{Mo})$  and  $N_\beta(^{108}\text{Nb})$  are the integral of mea-

sured <sup>108</sup>Mo and <sup>108</sup>Nb decays after the <sup>108</sup>Nb implantation, respectively. The neutron emission probability  $P_n$  is given by

$$P_n = 1 - P_{0n} = \sum_{i \geq 1} P_{in}, \quad (1)$$

where  $i$  is the number of the emitted neutrons.

$N_\beta(^{108}\text{Nb})$  was determined to be  $5.20(13) \times 10^4$  from a fit to the  $\beta$ -decay time curve obtained following the implantation of <sup>108</sup>Nb. The fit used the decay half-lives and neutron-emission probabilities of the parent <sup>108</sup>Nb, daughters <sup>107,108</sup>Mo, granddaughters <sup>106,107,108</sup>Tc and great granddaughters <sup>107,108</sup>Ru from the literature [34] except for <sup>108</sup>Nb where the half-life of 186(8) ms mea-

sured in this work was used. It was assumed that the probability of the emission of two or more neutrons is negligibly small so that  $P_{1n} = 1 - P_{0n}$ .

$N_\beta(^{108}\text{Mo})$  can be derived from the number of counts of the 268.3-keV  $\gamma$  ray,  $N_\gamma(268.3 \text{ keV})$ , emitted from the  $^{108}\text{Mo} \rightarrow ^{108}\text{Tc}$  decay using the relation,

$$N_\gamma(268.3 \text{ keV}) = N_\beta(^{108}\text{Mo})\varepsilon_\gamma(268.3 \text{ keV}) \times I_{\gamma,\text{abs}}(268.3 \text{ keV}), \quad (2)$$

where  $\varepsilon_\gamma(268.3 \text{ keV})$  is the  $\gamma$ -ray detection efficiency, which is sensitive to the implantation position, and  $I_{\gamma,\text{abs}}(268.3 \text{ keV})$  is the absolute intensity of 268.3 keV per one  $^{108}\text{Mo}$  decay. In order to evaluate  $N_\beta(^{108}\text{Mo})$ , we define the ratio,

$$R(268.3 \text{ keV}) = \frac{N_\gamma(268.3 \text{ keV})}{N_\beta(^{108}\text{Mo})}, \quad (3)$$

which should be the same for the  $^{108}\text{Nb} \rightarrow ^{108}\text{Mo} \rightarrow ^{108}\text{Tc}$  and  $^{108}\text{Mo} \rightarrow ^{108}\text{Tc}$  decays, if the position of the  $^{108}\text{Nb}$  and  $^{108}\text{Mo}$  parent in WAS3ABi is the same. To satisfy this requirement, we consider only events where the implanted ion is  $^{108}\text{Nb}$ . To obtain a value of  $R(268.3 \text{ keV})$  from the  $^{108}\text{Mo} \rightarrow ^{108}\text{Tc}$  decay, we use the detection time of the 192.8-keV  $\gamma$  ray emitted from the  $2_1^+$  state in  $^{108}\text{Mo}$  as a time-zero of the decay of  $^{108}\text{Mo}$ .  $N_\beta(^{108}\text{Mo})$  was then obtained from the  $\beta$ -decay time curve using the same method as described for  $^{108}\text{Nb}$ . The number of  $^{108}\text{Tc}$  268.3-keV  $\gamma$  rays was obtained from the  $\gamma$ -ray peak integral to give  $R(268.3 \text{ keV}) = 0.0558(65)$ .

To obtain a value of  $N_\gamma(268.3 \text{ keV})$  for the  $^{108}\text{Nb} \rightarrow ^{108}\text{Mo} \rightarrow ^{108}\text{Tc}$  decay, a time gate of 400–3000 ms after the  $^{108}\text{Nb}$  implantation in WAS3ABi was applied to optimize the  $\gamma$  rays emitted from the  $^{108}\text{Mo}$  decay. This yielded a 268.3-keV peak containing 1695(43) counts. The expected number of 268.3-keV  $\gamma$  rays observed without time restriction is evaluated as  $N_\gamma(268.3 \text{ keV}) = 2380(140)$ , which, using Eq. (3), equates to  $N_\beta(^{108}\text{Mo}) = 42700(5600)$ .

By using the relation,  $P_{0n} = \frac{N_\beta(^{108}\text{Mo})}{N_\beta(^{108}\text{Nb})}$ , we obtain  $P_{0n} = 82(11)\%$ , giving  $P_n = 18(11)\%$ . Observation of the known 65.4-keV  $\gamma$  ray [42] from the isomeric state in  $^{107}\text{Mo}$  in Fig. 4 (a) provides a direct evidence of the  $\beta$ -delayed neutron emission of  $^{108}\text{Nb}$ . The absolute  $\gamma$ -ray intensity of the 65.4-keV  $\gamma$  ray corresponds to a minimum  $P_{1n}$  of 8.1(7)%, which includes the contribution of the internal conversion for the E2 transition. It is reasonable that this is less than  $P_n = 18(11)\%$ , given above, as there exist unobserved one- or multi-neutron emission channels. The minimum value reported here is larger than a previously reported  $P_n$  value of 6.2(5)% [43] and equal to 8(2)% of Ref. [44]. The previous  $P_n$  values were derived from measurements of  $\beta$ -delayed neutrons with  $^3\text{He}$  ionization chamber tubes [43], or a combination of  $^3\text{He}$  and  $\text{B}_3\text{F}$  proportional gas-counter tubes [44]. Neutron-detection efficiencies of these configurations, which have a possible energy dependence, could have been affected by unknown  $\beta$ -delayed neutron energy distributions.

#### D. $\beta$ decay to $^{110}\text{Mo}$

The  $\beta$ -delayed  $\gamma$ -ray spectrum of  $^{110}\text{Mo}$  obtained from the  $\beta$  decay of  $^{110}\text{Nb}$  is shown in Figs. 6 (a–b), and the coincidence spectrum of the  $2_1^+ \rightarrow 0_1^+$  transition is shown in Fig. 6 (c). The proposed level scheme is shown in Fig. 7. In the previous works of the  $^{110}\text{Nb}$   $\beta$  decay and the  $^{248}\text{Cm}$  spontaneous fission decay [15, 45], the ground band up to  $10^+$  and the  $2_2^+$  band up to  $5^+$  were reported. In the present work, thirty new levels are identified and the  $2_2^+$  band is extended up to its  $7^+$  state. A new band based on a 1243.8-keV state was observed and from its interband transitions to the  $2_2^+$  band, a spin-parity of  $4^+$  was assigned to its band head. The spin-parities of the band members with 1520.1 keV and 1796.2 keV were assigned as  $5^+$  and  $6^+$ , respectively. A state at 1042.2 keV was measured based on the observation of a 828.8-keV  $\gamma$  ray coincident only with the 213.4-keV  $\gamma$  ray, as shown in Fig. 6 (d). Direct  $\gamma$  decay from the 1042.2-keV state to the ground state was not observed. Based on this typical  $\gamma$ -decay pattern of a low-lying  $0^+$  state, the 1042.2-keV state was assigned to  $0^+$ . The  $I_\gamma$  values are summarized in Table IV.

The  $\beta$ -delayed  $\gamma$ -ray spectrum of  $^{110}\text{Mo}$  obtained from the  $^{110}\text{Zr} \rightarrow ^{110}\text{Nb} \rightarrow ^{110}\text{Mo}$  decay chain is shown in Fig. 6 (e). Only five excited states were observed, which were the  $2^+$  and  $4^+$  states in the ground band, the  $2^+$  and  $3^+$  states in the  $2_2^+$  band, and the  $0_2^+$  state. This  $\beta$ -decay feeding pattern and the  $I_\gamma$  values, given in Table V, are different from those of the  $^{110}\text{Nb} \rightarrow ^{110}\text{Mo}$  decay. These differences indicate the existence of two  $\beta$ -decaying states in  $^{110}\text{Nb}$ . Since the spin-parity of the even-even nucleus  $^{110}\text{Zr}$  is  $0^+$ , it is expected that the low-spin states in  $^{110}\text{Nb}$  are populated by the  $\beta$  decay of  $^{110}\text{Zr}$ . This expectation is consistent with the  $\beta$ -decay feeding pattern to the lower-spin states in  $^{110}\text{Mo}$  by the  $^{110}\text{Zr} \rightarrow ^{110}\text{Nb} \rightarrow ^{110}\text{Mo}$  decay chain. On the other hand, the  $^{110}\text{Nb} \rightarrow ^{110}\text{Mo}$  decay has contributions of the low- and high-spin states in  $^{110}\text{Nb}$  because the in-flight fission reaction populates both states.

#### E. Extraction of $\beta$ -decay properties for low- and high-spin states in $^{110}\text{Nb}$

Beta-decay properties, namely  $T_{1/2}$ , relative and absolute  $\gamma$ -ray intensities,  $I_\beta$ , and  $\log ft$ , need to be determined separately for the low- and high-spin states in  $^{110}\text{Nb}$ . To evaluate  $T_{1/2}$  for the high-spin state, the  $\gamma$  rays with 462.6, 531.5, 563.3, and 563.4 keV from the  $5_1^+$ ,  $6_1^+$ , or  $6_2^+$  states were used as they are emitted only in the  $\beta$  decay of the high-spin state. The half-life of the high-spin state in  $^{110}\text{Nb}$  was determined to be 75(1) ms from the sum of the decay curves of these four  $\gamma$  rays using the data of the  $^{110}\text{Nb} \rightarrow ^{110}\text{Mo}$  decay as shown in Fig. 3 (c). The 213.4-keV  $\gamma$  ray obtained in the  $^{110}\text{Zr} \rightarrow ^{110}\text{Nb} \rightarrow ^{110}\text{Mo}$  decay chain was used for the half-life measurement of the low-spin state in  $^{110}\text{Nb}$ . The decay

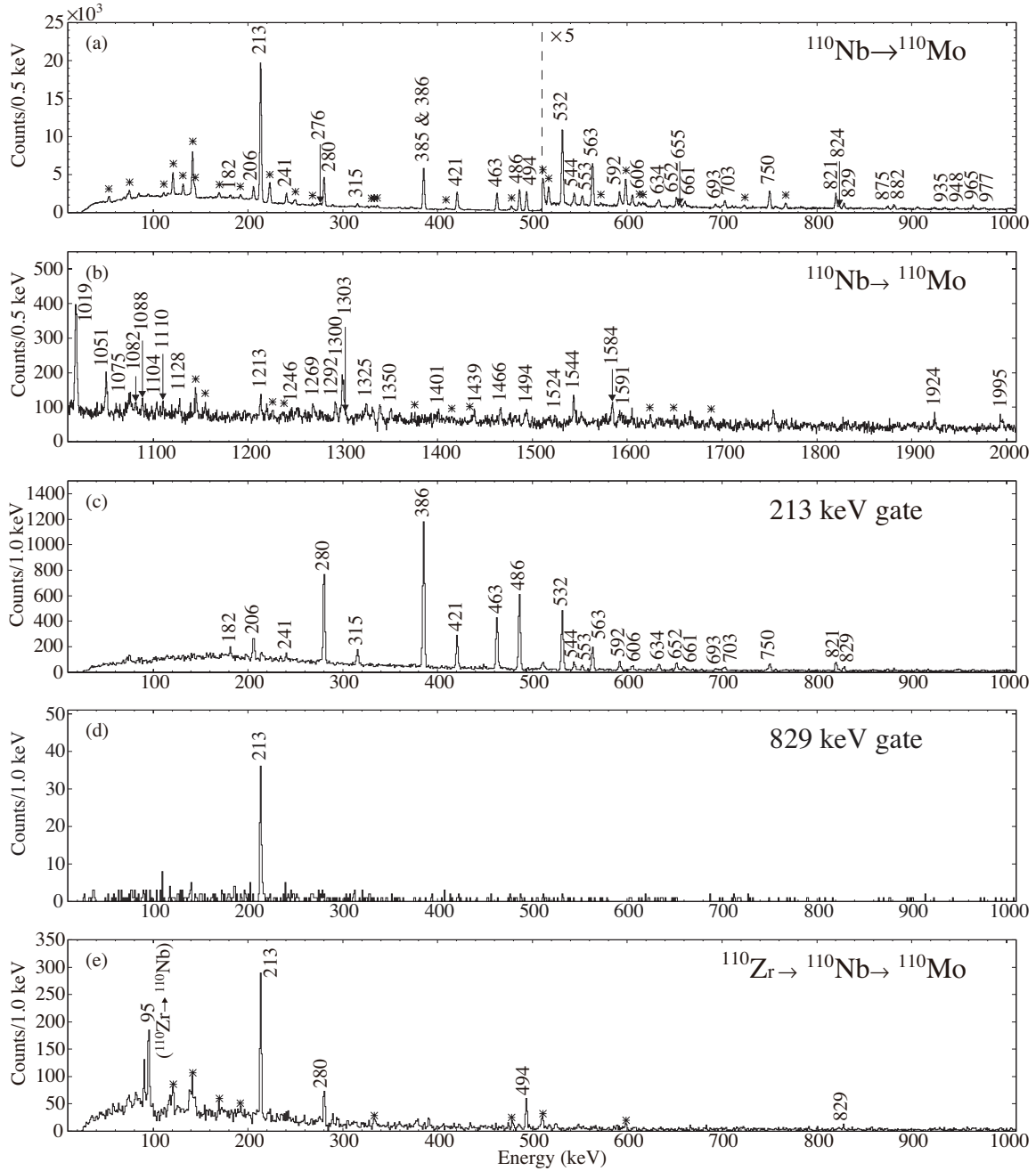


FIG. 6. (a–b) The  $\beta$ -delayed  $\gamma$ -ray spectrum of the implanted  $^{110}\text{Nb}$ . The time window after the implantation of  $^{110}\text{Nb}$  was set to be less than 400 ms. The labeled peaks belong to  $^{110}\text{Mo}$ . The identified background peaks are marked with asterisks. (c–d) The coincidence spectra gated on 213.4 keV and 828.8 keV. (e) The  $\beta$ -delayed  $\gamma$ -ray spectrum obtained from the  $\beta$ -decay chain  $^{110}\text{Zr} \rightarrow ^{110}\text{Nb} \rightarrow ^{110}\text{Mo}$ , where  $\Delta t_{\beta\text{-ion}}$  from 30 to 250 ms was selected.

curve shown in Fig. 3 (d) shows the typical shape of a daughter populated by the decay of a parent. The half-life of the low-spin state in  $^{110}\text{Nb}$  was determined to be 94(9) ms by considering the daughter-decay component and the constant background. The half-life of  $^{110}\text{Zr}$ , used in the fitting, was determined to be 37.7(31) ms from the decay curve of the 90.5- and 95-keV  $\gamma$  rays associated with the  $^{110}\text{Zr}$  decay. The half life of previous measure-

ments was determined without any consideration of the second  $\beta$ -decaying state in  $^{110}\text{Nb}$ . The previous values of 82(4) ms [34] and 82(2) ms [46] appear to be a reasonable average of the presently reported low- and high-spin states.

The absolute  $\gamma$ -ray intensities for the low-spin state in  $^{110}\text{Nb}$  were determined as follows. The  $\beta$  decay of  $^{110}\text{Nb}$  which followed the emission of a 95-keV  $\gamma$  ray from the

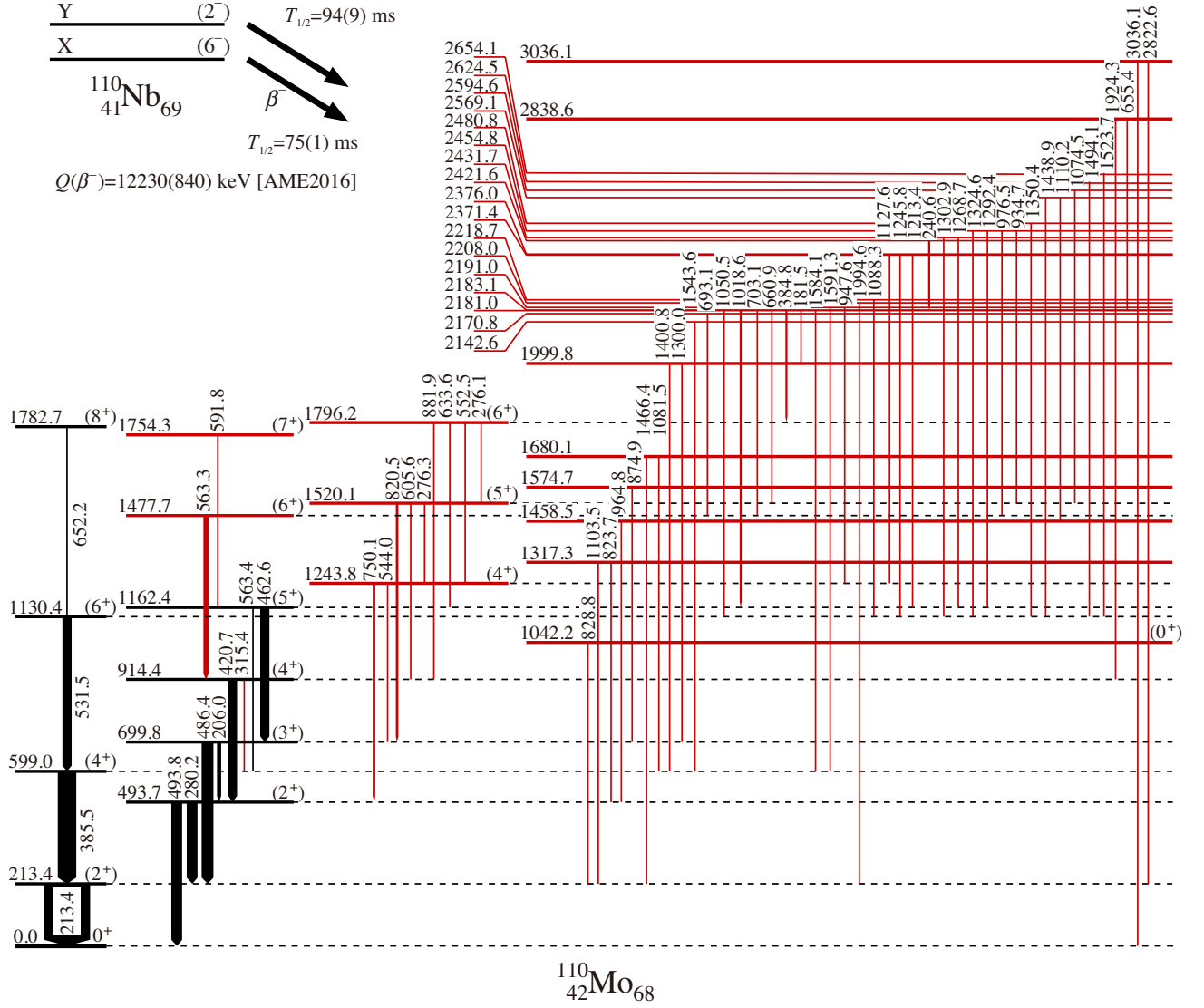


FIG. 7. The proposed level scheme of  $^{110}\text{Mo}$  obtained from the  $\beta$ -decay of  $^{110}\text{Nb}$  isotopes implanted into WAS3ABi. Red lines are the new levels and transitions.

TABLE IV: Same as Table II, but for the  $^{110}\text{Mo}$  results obtained from the  $\beta$  decay of the implanted  $^{110}\text{Nb}$ . (high) indicates the  $\beta$  decay of the high-spin state in  $^{110}\text{Nb}$ . The low-spin contribution was subtracted by combining with the results in Table V and the assumption that the  $0^+$  states at 0 and 1042.2 keV are populated only from the low-spin  $\beta$  decay. (1UF) is for the first unique forbidden transition from  $6^-$  to  $4^+$  or  $8^+$  states.

$E_i(\text{keV})$	$J^\pi$	$E_\gamma(\text{keV})$	$I_\gamma^a$ (Nb $\rightarrow$ Mo)	$I_\gamma^b$ (high)	$I_\beta(\%)^c$ (high)	$\log ft$ (high) (allowed/non-UF)	$\log ft$ (high) (1UF)
0.0	$0^+$				0		
213.4(2)	$(2^+)$	213.4(2)	100.0(5)	100(11)	<1.5		
493.7(1)	$(2^+)$	280.2(2)	23.5(4)	21.6(33)	-5.4(45)		
		493.8(2)	23.1(3)	18.9(38)			
599.0(2)	$(4^+)$	385.5(2)	39.0(7)	52.7(14)	6.2(16)	5.9(2)	8.5(3)
699.8(1)	$(3^+)$	206.0(2)	8.5(2)	11.3(3) <sup>e</sup>	1.5(6)	6.5(2)	
		486.4(2)	26.2(3)	34.9(8)			

TABLE IV: (continued)

$E_i$ (keV)	$J^\pi$	$E_\gamma$ (keV)	$I_\gamma^a$ (Nb→Mo)	$I_\gamma^b$ (high)	$I_\beta(\%)^c$ (high)	$\log ft$ (high) (allowed/non-UF)	$\log ft$ (high) (1UF)
914.4(2)	(4 <sup>+</sup> )	420.7(2)	18.8(3)	27.0(4)	4.8(15)	6.0(2)	8.5(3)
		315.4(2)	2.9(2)	4.2(3)			
1042.2(2)	(0 <sup>+</sup> )	828.8(2)	1.8(1)	0	0		
1130.4(3)	(6 <sup>+</sup> )	531.5(2)	19.7(3)	28.3(4)	8.2(20)	5.7(2)	
1162.4(2)	(5 <sup>+</sup> )	462.6(2)	19.7(3)	28.3(4)	6.5(17)	5.8(2)	
		563.4(3)	1.8(4)	2.6(6)			
1243.8(1)	(4 <sup>+</sup> )	544.0(2)	2.9(2)	4.2(3)	3.5(9)	6.1(2)	8.5(3)
		750.1(2)	5.9(2)	8.5(3)			
1317.3(2)		823.7(2)	1.3(1)	1.9(1)	1.4(3)	6.5(2)	
		1103.5(3)	0.5(1)	0.7(1)			
1458.5(2)		964.8(2)	1.1(1)	1.6(1)	0.5(2)	6.9(2)	
1477.7(2)	(6 <sup>+</sup> )	563.3(2)	10.0(10)	14.4(14)	4.8(14)	5.9(2)	
1520.1(2)	(5 <sup>+</sup> )	276.3(3)	0.3(4)	0.4(6)	3.8(11)	6.0(2)	
		605.6(2)	2.9(2)	4.2(3)			
		820.5(2)	4.9(2)	7.0(3)			
1574.7(3)		874.9(3)	0.9(1)	1.3(1)	0.7(2)	6.7(2)	
1680.1(2)		1081.5(3)	0.4(1)	0.6(1)	0.9(2)	6.6(2)	
		1466.4(3)	0.8(1)	1.2(1)			
1754.3(3)	(7 <sup>+</sup> )	591.8(2)	3.3(3)	4.7(4)	2.5(7)	6.1(2)	
1782.7(3)	(8 <sup>+</sup> )	652.2(2)	2.8(2)	4.0(3)	2.2(5)	6.2(2)	8.6(3)
1796.2(1)	(6 <sup>+</sup> )	276.1(3)	0.8(4)	1.2(6)	1.7(7)	6.3(2)	
		552.5(2)	2.7(2)	3.9(3)			
		633.6(2)	2.1(2)	3.0(3)			
		881.9(2)	1.6(1)	2.3(1)			
1999.8(2)		1300.0(2)	2.3(2)	3.3(3)	0.5(3)	6.8(3)	
		1400.8(4)	0.3(1)	0.4(1)			
2142.6(3)		1543.6(2)	1.6(2)	2.3(3)	1.2(3)	6.4(2)	
2170.8(3)		693.1(2)	0.9(1)	1.3(1)	0.7(2)	6.6(2)	
2181.0(1)		181.5(2)	1.9(2)	2.7(3)	10.1(25)	5.4(2)	
		384.8(2)	5.0(6)	7.2(9)			
		660.9(2)	1.4(1)	2.0(1)			
		703.1(2)	2.4(1)	3.5(1)			
		1018.6(2)	5.0(2)	7.2(3)			
		1050.5(2)	1.6(1)	2.3(1)			
2183.1(3)		1584.1(2)	1.4(2)	2.0(3)	0.4(2)	6.8(3)	
2191.0(3)		947.6(3)	0.6(1)	0.9(1)	1.0(3)	6.4(2)	
		1591.3(4)	0.7(2)	1.0(3)			
2208.0(4)		1994.6(3)	0.8(1)	1.2(1)	0.6(2)	6.6(2)	
2218.7(4)		1088.3(3)	0.5(1)	0.7(1)	0.4(1)	6.8(2)	
2371.4(4)		1127.6(3)	0.6(1)	0.9(1)	0.5(1)	6.7(2)	
2376.0(3)		1213.4(3)	0.9(1)	1.3(1)	0.9(2)	6.4(2)	
		1245.8(3)	0.3(1)	0.5(1)			
2421.6(2)		240.6(2)	4.2(7)	6.0(10)	3.2(9)	5.9(2)	
2431.7(3)		1268.7(3)	0.7(1)	1.0(1)	0.8(2)	6.5(2)	
		1302.9(6)	0.4(1)	0.6(1)			
2454.8(2)		934.7(3)	0.5(1)	0.7(1)	2.0(5)	6.1(2)	

TABLE IV: (continued)

$E_i$ (keV)	$J^\pi$	$E_\gamma$ (keV)	$I_\gamma^a$ (Nb→Mo)	$I_\gamma^b$ (high)	$I_\beta(\%)^c$ (high)	log $ft$ (high) (allowed/non-UF)	log $ft$ (high) (1UF)
		976.5(3)	0.4(1)	0.6(1)			
		1292.4(2)	1.0(1)	1.4(1)			
		1324.6(3)	0.7(1)	1.0(1)			
2480.8(4)		1350.4(3)	0.7(1)	1.1(1)	0.5(2)	6.7(3)	
2569.1(3)		1110.2(3)	0.4(1)	0.6(1)	0.8(2)	6.5(2)	
		1438.9(3)	0.6(1)	0.9(1)			
2594.6(5)		1074.5(5)	0.4(1)	0.6(1)	0.3(1)	6.9(2)	
2624.5(4)		1494.1(3)	0.9(3)	1.3(4)	0.7(3)	6.5(3)	
2654.1(4)		1523.7(3)	0.6(1)	0.9(1)	0.5(1)	6.6(2)	
2838.6(2)		655.4(2)	0.9(1)	1.3(1)	1.4(4)	6.2(2)	
		1924.3(3)	0.9(2)	1.3(3)			
3036.1(2)		2822.6(3)	1.1(1)	1.6(1)	2.1(5)	5.9(2)	
		3036.1(3)	1.6(2)	2.3(3)			

<sup>a</sup> The absolute intensity per 100  $\beta$ -decays is  $0.492(25)I_\gamma$ .

<sup>b</sup> The absolute intensity per 100  $\beta$ -decays is  $0.54(19)I_\gamma$ .

<sup>c</sup> Internal conversion coefficients [39] were adopted for two transitions with 213.4 and 206.0 keV.

<sup>e</sup> Branching ratio of the 206.0- and 486.4-keV transitions and  $I_\gamma$ (486.4 keV) in Table V were used to subtract the low-spin  $\beta$  decay contribution.

decay of  $^{110}\text{Zr}$  was analyzed using the observation of the 95-keV  $\gamma$  ray as time zero. The observation of the 213.4-, 280.2-, and 493.8-keV  $\gamma$  rays shows that the low-spin state in  $^{110}\text{Nb}$  is selected by the gate on the 95-keV  $\gamma$  ray. The ratio of the number of the measured  $\beta$  decays and 213.4-keV  $\gamma$  rays was determined from this subsequent  $\beta$ -decay analysis. The conversion factor from  $I_\gamma$  to absolute intensity was determined to be 0.41(14) using the 213.4-keV  $\gamma$  ray.

The  $I_\gamma$  values corresponding to the high-spin state were determined by subtracting the low-spin contribution from the results given in Table V under the assumption that the ground and second  $0^+$  states are directly populated only by the low-spin  $\beta$  decay. The  $I_\beta$  values for low- and high-spin  $\beta$  decays were determined and are summarized in Tables IV and V.

The  $I_\beta$  value of the  $^{110}\text{Mo}$  ground state corresponding to the low-spin state and  $P_n$  values corresponding to the low- and high-spin states were determined by combining the following five equations. First, the  $P_n$  value has a relation to  $I_\beta(E_i)$  for the  $\gamma$ -decaying states at the energy  $E_i$  and  $I_\beta(0)$  for the ground state as,

$$\sum I_\beta^L(E_i) + I_\beta^L(0) + P_n^L = 100\%, \quad (4)$$

$$\sum I_\beta^H(E_i) + P_n^H = 100\%, \quad (5)$$

where  $\sum$  represents the sum over all excited states decaying to the ground state and the superscripts L and H represent the low- and high-spin states in  $^{110}\text{Nb}$ , respectively. The  $\sum I_\beta^L(E_i)$  value was evaluated as 58(20)% by the sum of the two absolute transition intensities of

213.4 and 493.8 keV, which decay directly to the ground state. The conversion-electron coefficients were taken into account. This sum includes unobserved small  $I_\beta$  contributions with cascade transitions through the  $2_1^+$  and  $2_2^+$  states. The same method was applied to the  $\beta$ -decay results of the implanted  $^{110}\text{Nb}$ . The contribution of the 3036.1-keV transition was also added. The obtained value,  $\sum I_\beta^{L+H}(E_i) = 65.2(33)$ , includes the contribution of both the low- and high-spin states. The superscript L+H refers to the  $\beta$  decay of the implanted  $^{110}\text{Nb}$ . The  $\sum I_\beta^H(E_i)$  value was described by using the fraction  $r$  of the low-spin state in the implanted  $^{110}\text{Nb}$  as,

$$\sum I_\beta^{L+H}(E_i) = r \sum I_\beta^L(E_i) + (1-r) \sum I_\beta^H(E_i). \quad (6)$$

From the assumption that the 828.8-keV  $\gamma$  ray is emitted only from the  $\beta$  decay of the low-spin state,  $r$  was given as,

$$r = \frac{I_{\gamma,\text{abs}}^{L+H}(828.8 \text{ keV})}{I_{\gamma,\text{abs}}^L(828.8 \text{ keV})} = 0.36(15), \quad (7)$$

where  $I_{\gamma,\text{abs}}(828.8 \text{ keV})$  is the absolute intensity of the 828.8-keV  $\gamma$  ray.

From the data of the  $^{110}\text{Nb} \rightarrow ^{110}\text{Mo} \rightarrow ^{110}\text{Tc}$  decay chain, the  $P_{0n}^{L+H}$  value can be determined following the procedure described in Sec. III C. It is given by

$$1 - P_{0n}^{L+H} = rP_n^L + (1-r)P_n^H, \quad (8)$$

Here, only the differences from Sec. III C are described. The 213.4-keV  $\gamma$  ray was used for the identification of the  $^{110}\text{Nb} \rightarrow ^{110}\text{Mo}$  decay. The number



TABLE V. Same as Table II, but for the  $^{110}\text{Mo}$  results obtained from the  $\beta$ -decay chain  $^{110}\text{Zr} \rightarrow ^{110}\text{Nb} \rightarrow ^{110}\text{Mo}$ , where the low-spin state in  $^{110}\text{Nb}$  is populated by the  $\beta$  decay of the  $0^+$  ground state in  $^{110}\text{Zr}$ . (1UF) is for the first unique forbidden transition from  $2^-$  to  $0^+$  or  $4^+$  states.

$E_i$ (keV)	$J^\pi$	$E_\gamma$ (keV) (low)	$I_\gamma^a$ (low)	$I_\beta$ (%) (low)	$\log ft$ (low) (allowd/non-UF)	$\log ft$ (low) (UF)
0.0	$0^+$			47(26)	5.2(3)	7.8(4)
213.4	$(2^+)$	213.4	100(4)	25.0(88)	5.5(2)	
493.7	$(2^+)$	280.2	28.0(24)	25.0(87)	5.4(2)	
		493.8	33.0(27)			
599.0	$(4^+)$	385.5	7.0(13)	2.9(11)	6.4(2)	8.9(3)
699.8	$(3^+)$	486.4	6.0(4)	2.5(9)	6.4(2)	
1042.2	$(0^+)$	828.8	6.0(15)	2.5(10)	6.3(2)	8.8(3)

<sup>a</sup> The absolute intensity per 100  $\beta$  decays is  $0.41(14)I_\gamma$ .

of the  $^{110}\text{Mo}$   $\beta$  decay was obtained using the 121.0-keV  $\gamma$  ray emitted from  $^{110}\text{Tc}$ . From  $R(121.0 \text{ keV}) = 0.0375(16)$ ,  $N_\gamma(121.0 \text{ keV}) = 2.279(44) \times 10^4$ , and  $N_\beta(^{110}\text{Nb}) = 7.39(7) \times 10^5$ ,  $P_{0n}^{L+H} = 82(4)\%$  and  $P_n^{L+H} = 18(4)\%$  were determined.

Based on the above values and Eqs. (4–8), the remaining values were determined as  $P_n^L = -5(41)\%$ ,  $P_n^H = 31(15)\%$ ,  $I_\beta^L(0) = 47(26)\%$ , and  $\Sigma I_\beta^H(E_i) = 69(15)\%$ . Since the  $P_n^L$  value must be positive, an upper limit is given as  $P_n^L < 36\%$ . The large uncertainties were propagated mainly from the uncertainty of  $I_{\gamma,\text{abs}}^L(828.8 \text{ keV})$ . The separate  $P_n$  determination of the low- and high-spin states was made for the first time in the  $^{110}\text{Nb}$   $\beta$  decay. The previous  $P_n^{L+H}$  value of  $40(8)\%$  [43] is larger than the present result. In the previous work,  $^{110}\text{Nb}$  was produced by bombarding a U target with a 50 MeV  $\text{H}_2^+$  beam. The low-spin fraction  $r$  may be different due to the different production reaction and energy.

The  $\log ft$  values were determined from the half-lives,  $I_\beta$  and  $Q_\beta = 12230(840) \text{ keV}$  [33] for the low- and high-spin states, (as summarized in Tables IV and V), respectively. The excitation energy in  $^{110}\text{Nb}$  was not taken into account, which would be negligible in comparison with its  $Q_\beta$ .

First, the spin-parity of the low-spin state in  $^{110}\text{Nb}$  is discussed. Positive-parity states with spins ranging from 0 to 4 are populated by the  $\beta$  decay of the low-spin  $^{110}\text{Nb}$ . Because this decay pattern and the  $\log ft$  values are similar to the  $^{108}\text{Nb}$  decay, the spin-parity of the low-spin  $^{110}\text{Nb}$  is assigned to be  $2^-$ . The  $\log ft$  values of  $0^+$  and  $4^+$  states were recalculated as the first unique forbidden transition to be 7.8(4), 8.8(3), and 8.9(3) for  $0_1^+$ ,  $0_2^+$ , and  $4_1^+$ , respectively. These are consistent with the typical range from 8 to 11 [40].

For the  $\beta$  decay from the high-spin state, it is impossible to interpret the  $\log ft$  values of both the  $3^+$  and  $8^+$  states, even if the first unique forbidden transition is considered. Because the  $I_\beta$  to the  $3^+$  state, 1.5(6), is smaller than the other states, missing feedings from

higher excited states may cause a significant deviation from the actual  $\log ft$ . On the other hand, it is reasonable that the  $8^+$  state, which is the largest spin among the measured states, is directly populated. Therefore, the  $3^+$  state is considered to be mainly fed from the higher excited states. The  $\log ft$  values of the  $4^+$ ,  $5^+$ ,  $6^+$ ,  $7^+$ , and  $8^+$  states are in the range from 5.7 to 6.3. This case is similar to the situation above. When the spin-parity of the high-spin state in  $^{110}\text{Nb}$  is  $6^-$ , the transitions to  $4^+$  or  $8^+$  states become the first unique forbidden transition. The recalculated  $\log ft$  values, 8.5(3), 8.5(3), 8.5(3) and 8.6(3) for the  $4_1^+$ ,  $4_2^+$ ,  $4_3^+$ , and  $8_1^+$  states, respectively, are consistent with the typical range. For the other positive parity states, the  $\log ft$  values are consistent with the first non-unique forbidden transitions from the  $6^-$  state. As a result, the spin-parity of the high-spin state is assigned to be  $6^-$ .

#### F. Lifetime measurement of $2_1^+$ states in $^{106,108,110}\text{Mo}$

The mean lifetimes,  $\tau$ , of the  $2_1^+$  states in  $^{106,108,110}\text{Mo}$  were measured from the time between the observation of a  $\beta$  particle in a plastic scintillation detector and a  $\gamma$  ray corresponding to the  $2_1^+ \rightarrow 0_1^+$  transition in the  $\text{LaBr}_3(\text{Ce})$  detector array. Figure 8 shows the time-difference distributions for the three nuclei and Fig. 9 shows the corresponding  $\gamma$ -ray spectra with the regions used to make the time spectra highlighted in gray. The time spectra show a clear single exponential decay on a very low background. The  $\gamma$ -ray spectra in Fig. 9 do not show any evidence for delayed feeding of the  $2_1^+$  state from higher-lying states and indeed, the lifetime of the  $4_1^+$  state in  $^{108}\text{Mo}$  was recently measured as  $\tau = 29.7_{-9.1}^{+11.3}$  ps [9]. Its effect can be ignored, since the lifetime is one order of magnitude smaller than the time resolution of 0.61 ns at 200 keV. The lifetimes of the  $2_1^+$  states were determined from fitting the slope with a single ex-

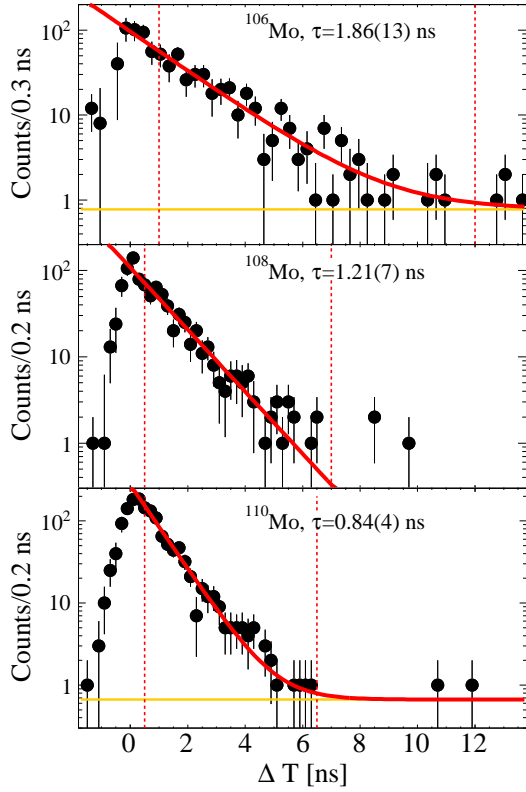


FIG. 8. The time spectra of  $2_1^+ \rightarrow 0_1^+$   $\gamma$ -ray transition in  $^{106}\text{Mo}$ ,  $^{108}\text{Mo}$ , and  $^{110}\text{Mo}$ .  $\Delta T$  is the time from  $\beta$ -particle detection by the plastic scintillator to  $\gamma$ -ray detection by the  $\text{LaBr}_3(\text{Ce})$  array. The solid red lines are the best-fit curves using an exponential function and fixed constant background to the region indicated by the dashed red lines. The constant backgrounds, shown by the orange lines, were determined by fitting the region of  $15 < \Delta T < 25$  ns,  $10 < \Delta T < 25$  ns, and  $8 < \Delta T < 25$  ns for  $^{106}\text{Mo}$ ,  $^{108}\text{Mo}$ , and  $^{110}\text{Mo}$ , respectively.

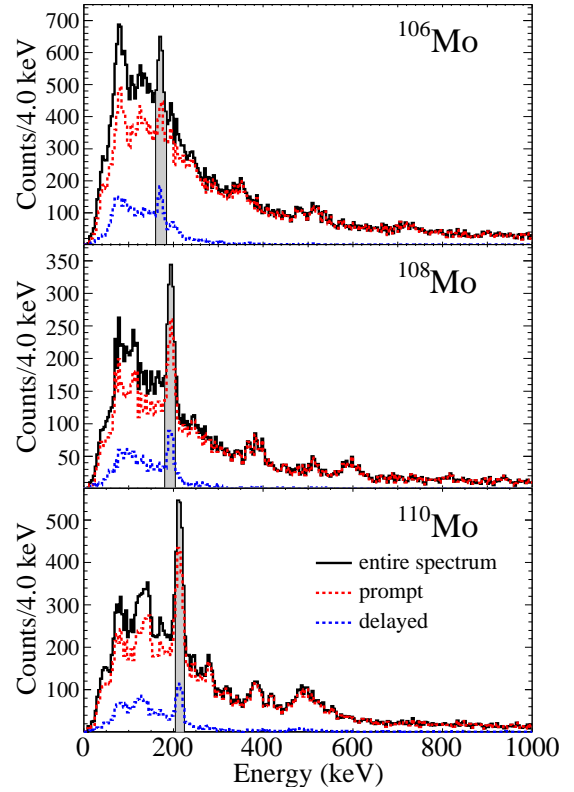


FIG. 9. The  $\gamma$ -ray energy spectra of the  $\text{LaBr}_3(\text{Ce})$  array. The energy region used to make the time spectra of Fig. 8 are highlighted with gray. The prompt,  $|\Delta T| < 1$  ns, and delayed,  $\Delta T > 1$  ns, components are shown by the red and blue dotted lines, respectively.

#### IV. DISCUSSION

##### A. Quadrupole deformation of ground state in $^{106,108,110}\text{Mo}$

The ground-state band is described as the rotational motion of a deformed nucleus. The quadrupole deformation parameter  $\beta$  was obtained from the  $B(E2; 2_1^+ \rightarrow 0_1^+)$  values using the formula given in the review paper [48] as 0.349(13), 0.327(10), and 0.305(7) for  $^{106}\text{Mo}$ ,  $^{108}\text{Mo}$ , and  $^{110}\text{Mo}$ , respectively. Figure 11 shows the neutron-number dependence of  $\beta$  for Mo and Zr isotopes. While the Zr isotopes have a clear peak structure at  $N = 64$  and reach  $\beta = 0.46(1)$ , the Mo isotopes have almost constant  $\beta \sim 0.32$  between  $N = 60$  and 68. A comparison with microscopic calculations is described in Sec. IV E.

##### B. Triaxial motion in $2_2^+$ band

The low-lying  $2_2^+$  state is a signature of a softness against  $\gamma$  vibration, a  $\gamma$ -unstable rotor, or a rigid triaxial rotor. The three models are distinguished by means of

ponential function and a constant background, yielding  $\tau = 1.86(13)$ ,  $1.21(7)$ , and  $0.84(4)$  ns for  $^{106}\text{Mo}$ ,  $^{108}\text{Mo}$ , and  $^{110}\text{Mo}$ , respectively. The previously reported results for  $^{106}\text{Mo}$  are 0.54(8) [47, 48], 1.08(22) [49], 1.73(24) [50], and 1.93(14) ns [51]. The present lifetime ( $\tau = 1.86(13)$  ns) is consistent with the values in Refs. [50, 51]. The result of  $\tau = 1.21(7)$  ns for  $^{108}\text{Mo}$  is consistent with the previously reported value of 0.72(43) ns [21] but provides a smaller uncertainty. The measurement for  $^{110}\text{Mo}$  was made for the first time. The systematic trend of  $B(E2; 2_1^+ \rightarrow 0_1^+)$  values in the Mo isotopes is shown in Fig. 10. The present results with small uncertainties show that the  $B(E2)$  value is nearly unchanged between the neutron numbers  $N = 62$  and 66, and drops slightly at  $N = 68$ .

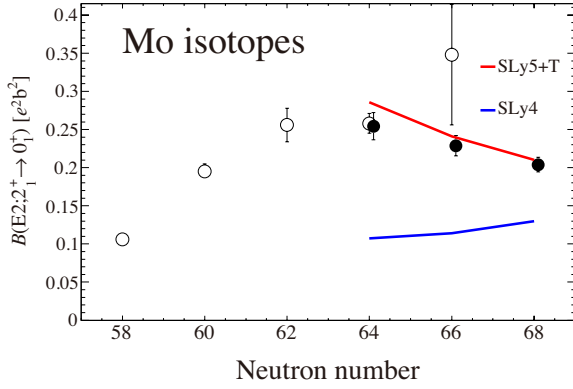


FIG. 10. Experimental and theoretical  $B(E2; 2_1^+ \rightarrow 0_1^+)$  values of the even-even Mo isotopes. The experimental values were calculated by the use of the relation in Ref. [52]. The open circles are taken from Ref. [48]. The theoretical values were calculated using the five-dimensional collective Hamiltonian with the pairing-plus-quadrupole interaction parameters determined from the two kinds of the Skyrme-interaction parameters (SLy5+T and SLy4).

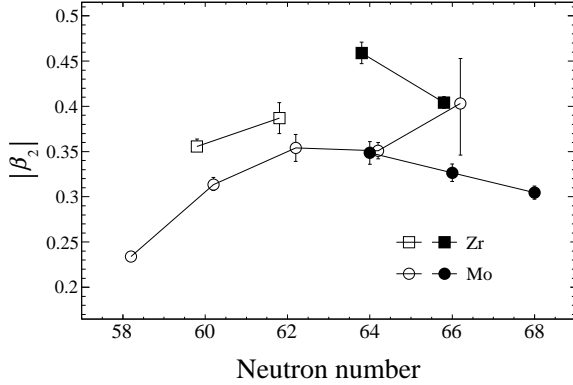


FIG. 11. Quadrupole deformation parameter  $\beta$  for Zr (square) and Mo (circle) isotopes. Filled circles are the present results for the Mo isotopes. Filled squares for the Zr isotopes are the results from the same data set [53], but the values were recalculated from  $B(E2; 2_1^+ \rightarrow 0_1^+)$  by using the formula given in the review paper [48]. Open circles and squares are taken from the review paper [48] and a later work [54].

the energy staggering of the  $2_2^+$  band [1]:

$$\frac{E_s(J)}{E(2_1^+)} = \frac{\Delta E_J - \Delta E_{J-1}}{E(2_1^+)}, \quad (9)$$

where  $\Delta E_J = E_\gamma(J) - E_\gamma(J-1)$ , and  $E_\gamma(J)$  is the energy of the  $2_2^+$  band member with the spin  $J$ . The  $E_s(4)/E(2_1^+)$  value of the  $\gamma$ -vibrational band is close to  $1/3$ , which is given by the  $J(J+1) - K^2$  rule if the rotational energies are described approximately as the axially-symmetric rigid rotor. At maximum triaxiality ( $\gamma = 30^\circ$ ) of a rigid-triaxial rotor in the Davydov model, it becomes  $5/3$  [2]. Another extreme case of  $\gamma$ -unstable nuclei in the Wilets-Jean model [3] yields  $-2$ . Figure

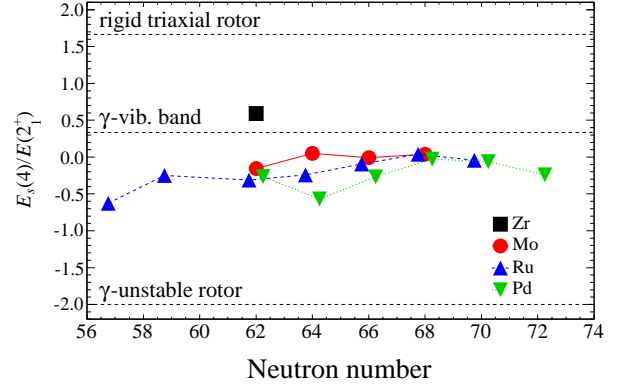


FIG. 12. The  $E_s(4)/E(2_1^+)$  ratio around neutron-rich  $A = 110$ . The black-dashed lines represent the ideal values of three models; rigid-triaxial rotor,  $\gamma$ -unstable rotor, and  $\gamma$ -vibrational band. Filled square, circles, triangles and inverted triangles represent Zr, Mo, Ru, and Pd isotopes, respectively.

12 shows the  $E_s(4)/E(2_1^+)$  ratio around the neutron-rich  $A = 110$  region. The Mo, Ru, and Pd isotopes have similar values in the range from  $-0.5$  to  $+0.1$ , which is below the  $1/3$  of the  $\gamma$  vibrational band. A larger value of  $^{102}\text{Zr}$  than other isotopes suggests that  $^{102}\text{Zr}$  has the steeper potential towards the  $\gamma$  direction.

Figure 13 shows the  $E_s(J)/E(2_1^+)$  ratio as a function of  $J$  for the Mo, Ru, and Pd isotopes. The difference among the isotopes is more apparent than in Fig. 12. The  $J$ -dependence of  $E_s(J)/E(2_1^+)$  is shown to have a relation to the triaxial motion from the calculation using the Bohr Hamiltonian with a  $\gamma$ -dependent potential [4]. While the  $\gamma$ -vibrational band shows a flat pattern, the  $\gamma$ -soft and the rigid triaxial rotors show a staggering pattern with low values at even and odd  $J$ , respectively. The flat pattern of the  $^{106,108,110}\text{Mo}$  isotopes indicates that the excitation energies are explained by the rotational bands built on a  $\gamma$ -vibrational  $2_2^+$  state with the axially-symmetric deformed shape and quantum number  $K = 2$ . On the other hand, the staggering pattern of the Pd isotopes with  $N \leq 66$  indicates a  $\gamma$ -soft rotor. The Ru isotopes show an intermediate behavior. The staggering pattern of the Pd isotopes suddenly disappears at  $N = 68$ . Especially at  $J \geq 6$ , a slight staggering in the opposite direction is observed. It is observed that the three isotopes with  $N = 68$  show a similar staggering pattern to each other. This staggering is enhanced for  $^{112}\text{Ru}$ . The staggering pattern at  $N = 68$  might indicate the onset of a very weak triaxial shape and might show a significant neutron contribution to make a shallow potential minimum at a finite  $\gamma$ .

For the  $\gamma$ -vibrational band, the kinematic moment of inertia (MoI) is expected to be similar to that of the ground band. Figure 14 shows the kinematic MoI of the ground and  $2_2^+$  bands up to  $J = 10$ . The newly discovered levels in the  $K = 2$  band of  $^{110}\text{Mo}$  extended the kinematic MoI up to  $J = 7$ . The similar evolution of the kinematic MoI between these two bands supports the interpretation

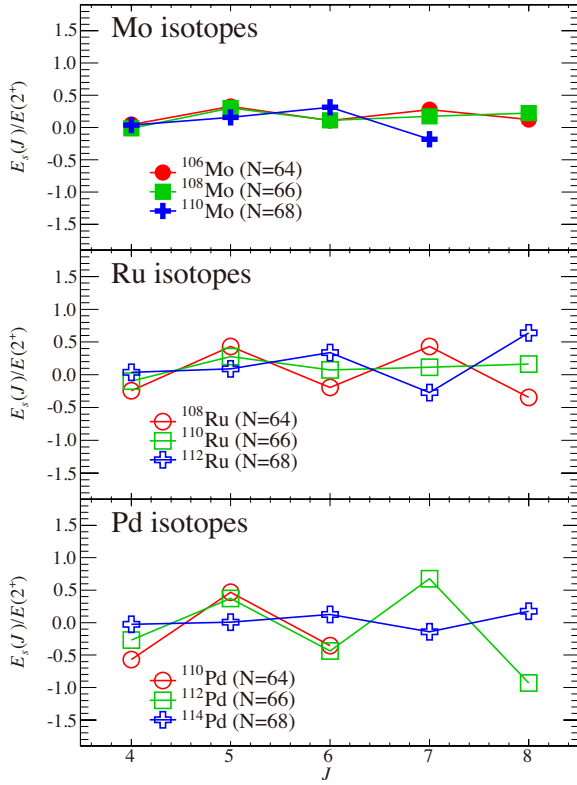


FIG. 13. The staggering pattern of  $E_s(J)/E(2_1^+)$ . The flat pattern indicates the  $\gamma$ -vibrational band, while the staggering pattern with low values at even and odd  $J$  indicates the  $\gamma$ -soft and rigid triaxial rotor, respectively, [4].

TABLE VI. The experimental and theoretical  $B(E2)$  ratios. The M1/E2 mixing ratio of  $\delta = 6.2^{+1.0}_{-0.8}$  [56] was used for  $^{106}\text{Mo}$ . A pure E2 transition was assumed for  $^{108}\text{Mo}$  and  $^{110}\text{Mo}$ . The theoretical calculation using the SLy5+T interaction is given.

	Alaga	$^{106}\text{Mo}$	$^{108}\text{Mo}$	$^{110}\text{Mo}$
$B(E2; 2_2^+ \rightarrow 2_1^+)$				
$B(E2; 2_2^+ \rightarrow 0_1^+)_{\text{exp.}}$		4.5(6)	8.3(6)	17.3(4)
$B(E2; 2_2^+ \rightarrow 2_1^+)_{\text{th.}}$	1.43	2.0	4.9	14.0

of a  $\gamma$ -vibrational band.

The ratio  $B(E2; 2_2^+ \rightarrow 2_1^+)/B(E2; 2_2^+ \rightarrow 0_1^+)$  provides additional information about the  $2_2^+$  band. The  $B(E2)$  ratio is given as 1.43 by the Alaga rule [55], where the rotational and vibrational motions for the axially-symmetric shape are well decoupled. The experimental  $B(E2)$  ratios shown in Table VI are clearly larger than the Alaga value. For the  $\gamma$ -vibrational band, the enhancement can be explained by the rotation-vibration coupling model which introduces the Coriolis mixing between two bands with  $\Delta K = 2$  [1]. In Sec. IV E, the  $B(E2)$  ratio is compared with beyond-mean-field calculations.

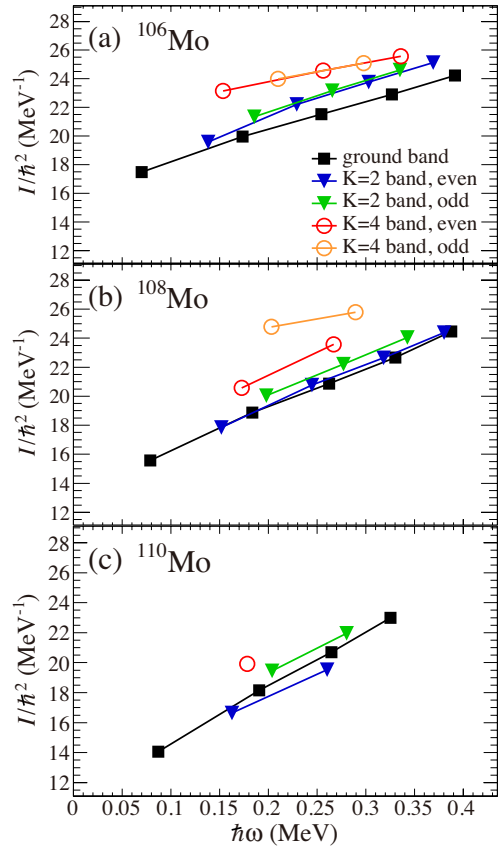


FIG. 14. The kinematic moment of inertia for the ground band (black line with filled squares),  $K^\pi = 2^+$  band (blue line with filled triangles for even  $J$  and green line for odd  $J$ ), and  $K^\pi = 4^+$  band (red line with open circles for even  $J$  and orange line for odd  $J$ ) in (a)  $^{106}\text{Mo}$ , (b)  $^{108}\text{Mo}$ , and (c)  $^{110}\text{Mo}$ .

### C. Candidate of two-phonon $\gamma$ band

The  $K^\pi = 4^+$  band in  $^{110}\text{Mo}$  has the lowest band-head energy of 1244 keV among the neutron-rich Mo isotopes. A potential two-quasiparticle state with  $K^\pi = 4^+$  would appear around or above the pairing gap. However, the observed energy is well below  $2\Delta_p \sim 3.4$  MeV and  $2\Delta_n \sim 2.5$  MeV for the proton and neutron pairs, respectively, which are calculated from the atomic mass evaluation AME2016 [33]. A  $K^\pi = 4^+$  band, decaying to the  $\gamma$  band, is known in many neighboring nuclei, such as  $^{104,106,108}\text{Mo}$ , and  $^{108,110,112,114,116}\text{Ru}$  [34, 57]. The systematical observations of the  $K^\pi = 4^+$  state indicate that the  $K^\pi = 4^+$  band head is a collective excitation rather than a two quasiparticle state.

The  $K^\pi = 4^+$  band in  $^{106}\text{Mo}$  has been discussed in the context of a two-phonon  $\gamma$  vibration [13]. The ratio of the lowest  $K^\pi = 4^+$  and  $2^+$  band-head energies is 2.02, which is close to the 2.0 value for a harmonic vibrator. The reduced transition probabilities of the interband transition between  $K^\pi = 2^+$  and  $4^+$  bands were compared with those between  $K^\pi = 0^+$  and  $2^+$  bands,

and were consistent with the relation of the one-phonon and two-phonon excitations. The ratio of the band-head energies changes gradually as 1.95, 2.02, 2.43, and 2.52 for  $^{104}\text{Mo}$ ,  $^{106}\text{Mo}$ ,  $^{108}\text{Mo}$ , and  $^{110}\text{Mo}$ , respectively. The kinematic MoI of the  $K^\pi = 4^+$  band shown in Fig. 14 has similar values to those of the ground-state and  $\gamma$  bands. Thus, the newly discovered  $K^\pi = 4^+$  band in  $^{110}\text{Mo}$  was assigned as a candidate of the two-phonon  $\gamma$  vibrational band.

#### D. Second $0^+$ state

The energies of the  $0_2^+$  state, 893.4 and 1042.2 keV for  $^{108}\text{Mo}$  and  $^{110}\text{Mo}$ , respectively, are low enough to indicate a  $\beta$ -vibrational state or shape coexistence rather than two-quasiparticle states, since they are well below the pairing gaps,  $2\Delta_p$  and  $2\Delta_n$ , given in Sec. IV C. The energies are similar to those of other Mo isotopes, which range from 695 keV to 886 keV between  $^{98}\text{Mo}$  and  $^{104}\text{Mo}$ , respectively [34].

The 1158.4-keV  $2^+$  state in  $^{108}\text{Mo}$  has a similar decay pattern to the  $2_3^+$  state in  $^{106,108,110}\text{Ru}$  isotopes [34]. The  $2_3^+$  state in the Ru isotopes decays also to the  $0_2^+$  state. Although the corresponding  $\gamma$ -ray transition from 1158.4-keV state to  $0_2^+$  state in  $^{108}\text{Mo}$  was not observed due to the lack of the sensitivity for  $I_\gamma < 0.5\%$ , the energy difference,  $E(2_3^+) - E(0_2^+) = 265$  keV, is similar to the cases of 402, 273, and 260 keV for  $^{106,108,110}\text{Ru}$  [34], respectively. Based on these systematic trends, the 1158.4-keV state in  $^{108}\text{Mo}$  was tentatively assigned as the member of the  $0_2^+$  band.

The  $0_2^+$  states of  $^{108,110}\text{Mo}$  will be discussed by comparing with predictions in Sec. IV E.

#### E. Comparison with 5D collective Hamiltonian calculation with microscopic approach

Five-dimensional collective Hamiltonian calculations were performed for the low-lying states in  $^{106,108,110}\text{Mo}$ . The PES and the kinetic terms (vibrational and rotational masses) were microscopically calculated using the CHFB+LQRPA approach using pairing-plus-quadrupole (P+Q) interactions whose parameters, such as spherical single-particle energies in the two-major harmonic oscillator shell model space and interaction strengths, were fitted to the mean-field results obtained with two kinds of Skyrme interactions, SLy5+T or SLy4 (see Refs. [58–60] for details). The Schrödinger equation in the collective space was solved to obtain the energies and the collective wave functions of the ground and excited states. The PESs and the collective wave functions squared are shown in Fig. 15 for SLy5+T and Fig. 16 for SLy4. The two kinds of theoretical excitation energies are compared with the experimental ones in Fig. 17. The PESs show a strong dependence on the effective interaction used. The calculation with the SLy5+T interaction predicts a pro-

late shape with  $\beta \sim 0.35$  and  $\gamma = 0^\circ$ , while the SLy4 interaction predicts an oblate shape with  $\beta \sim 0.2$  and  $\gamma = 60^\circ$ . For the comparison with the experimental results, the  $B(E2; 2_1^+ \rightarrow 0_1^+)$  value was used instead of  $\beta$ . The  $B(E2; 2_1^+ \rightarrow 0_1^+)$  values were calculated by adopting the effective charges,  $e_\pi = 1.5e$ , and  $e_\nu = 0.5e$ , for the two major-shell single-particle model space as shown in Fig. 10. The theoretical values with SLy5+T are roughly double those with SLy4 and agree well with the experimental ones. The energy of  $2_1^+$  state for the rotational band, which has a strong correlation to  $B(E2)$  [52], is an observable closely related to  $\beta$ . The energies of the ground-state band are well reproduced by the calculations with SLy5+T, as shown in Fig. 17. The good agreement with the theoretical values using the SLy5+T interaction indicates that the ground state in  $^{106,108,110}\text{Mo}$  has a prolate shape. The  $B(E2)$  values for SLy5+T shows an increase at  $N = 64$ , while the experimental ones are rather constant. The PES of  $^{106}\text{Mo}$  has a gentle slope toward  $\beta \sim 0.45$ , which may increase  $\beta$  compared with  $^{108}\text{Mo}$ . Because the largest  $\beta$  was observed at  $N = 64$  in the Zr isotopes [53] and the energy of the  $2_1^+$  state becomes minimum at  $N = 64$  for both isotopes [61], the soft potential toward the large  $\beta$  might be consistent with the experimental results. But a less-soft potential would be necessary for a better agreement.

The energies of the  $2_2^+$  band in  $^{106}\text{Mo}$  are well reproduced by the calculation with SLy5+T. The wave functions of  $2_\gamma^+$  and  $3_\gamma^+$  are localized on a finite  $\gamma$  value, reflecting the dynamical triaxial deformation induced by the  $\gamma$  vibration of the prolate shape. While the band-head energy in  $^{108}\text{Mo}$  is overestimated, the excitation energies measured with respect to the  $2_2^+$  state are well reproduced and the wave functions show the  $\gamma$  vibration expected from the experimental odd-even staggering. Thus, the calculations for  $^{106}\text{Mo}$  and  $^{108}\text{Mo}$  are consistent with the interpretation in Sec. IV B, that is, the rotational band of the  $\gamma$  vibrational state. On the other hand, the calculated  $2_2^+$  band in  $^{110}\text{Mo}$  shows considerable energy staggering. The  $3_\gamma^+$  and  $5_\gamma^+$  states converge toward the  $4_\gamma^+$  and  $6_\gamma^+$  states, respectively. The degeneracy of these states is predicted in the  $\gamma$ -unstable model. The wave function of  $2_\gamma^+$  is prolonged in the  $\gamma$  direction as expected in the  $\gamma$ -unstable model. It is caused by the flatness of the PES between  $\gamma = 20^\circ$  and  $60^\circ$ . Conversely, the experimental results indicate  $\gamma$  vibration in the stiffer potential. It is noticed that the calculated wave function of the  $3_\gamma^+$  state is similar to those of the lighter Mo isotopes and indicates  $\gamma$  vibration. The characteristics of the wave functions with higher spins change depending on if the spin is even or odd. This is also noticed in the calculations with SLy4. It is suggested that the energy staggering with the close degeneracy of  $E(3_\gamma)$  and  $E(4_\gamma)$  might depend not only on the prolonged wave function toward the  $\gamma$  direction, but also on the difference between the even and odd spins. The odd-spin states cannot mix with the  $K^\pi = 0^+$  component, since the odd-spin states are not allowed in the  $K^\pi = 0^+$  band. This means that the ex-

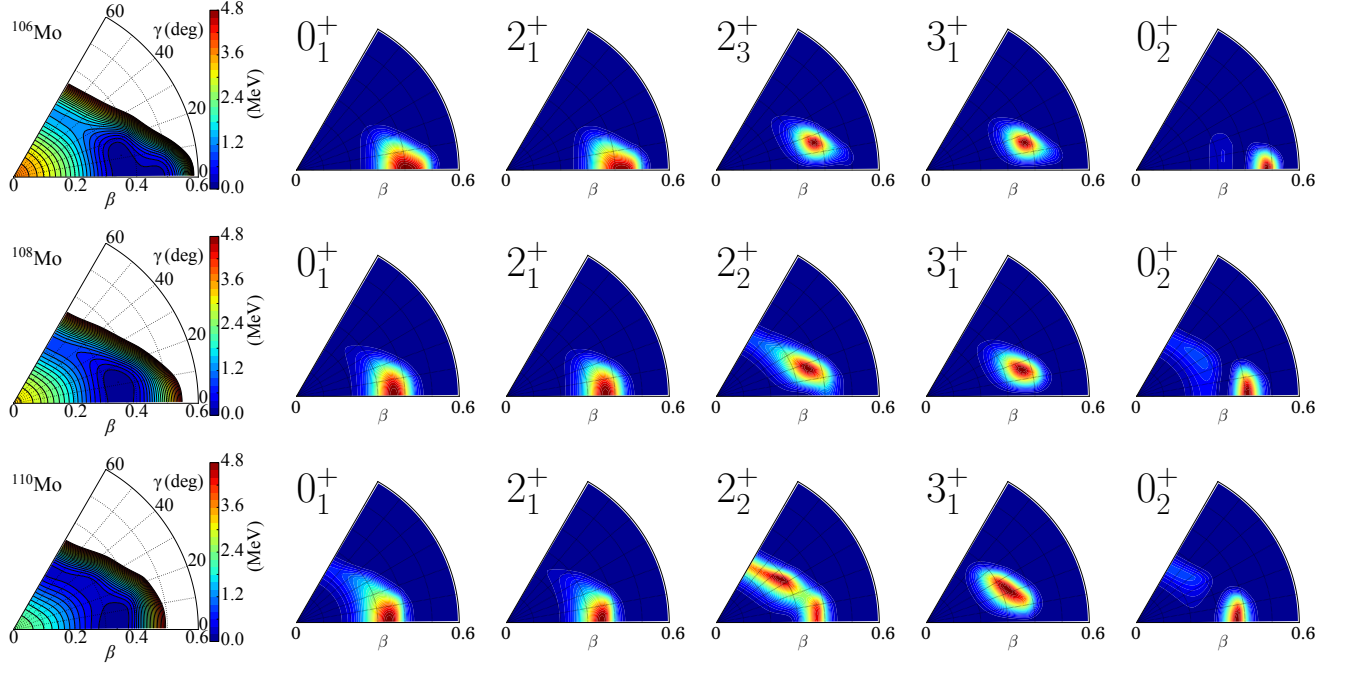


FIG. 15. The potential-energy surface and the collective-wave functions squared (with a factor of  $\beta^4$ ) of low-lying states in  $^{106}\text{Mo}$ ,  $^{108}\text{Mo}$ , and  $^{110}\text{Mo}$ . The pairing-plus-quadrupole interaction and spherical single-particle energies used in the CHFB+LQRP calculations were fitted to the mean-field results obtained with the SLy5+T interaction.

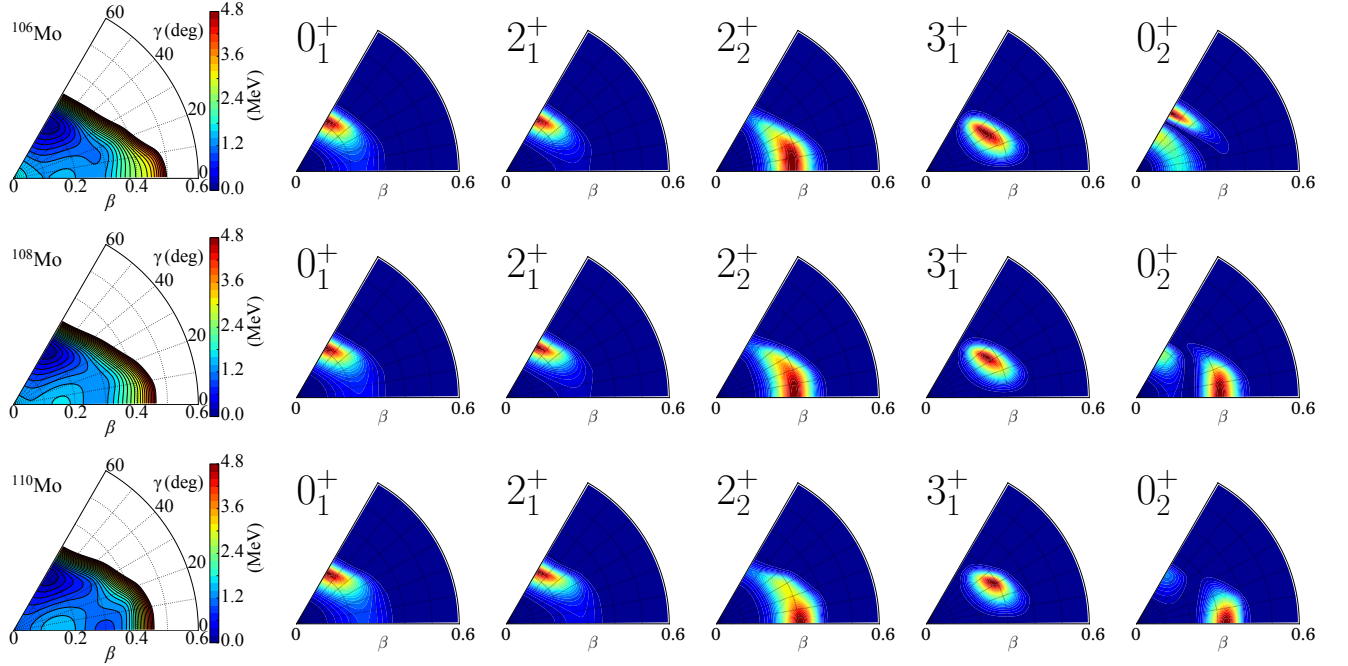


FIG. 16. Same as Fig. 15, but with the SLy4 interaction.

893 cited even-spin states (e.g.  $4_2^+$ ) are more influenced by 898 at all. This will result in a qualitative difference between  
 894 the mixing with  $K^\pi = 0^+$  bands, which are built on the 899 the even- and odd-spin states, and energy staggering that  
 895 ground state, shape coexistence, shape fluctuation in the 900 deviates from the ideal  $\gamma$ -band energy.  
 896  $\beta$  direction around  $\gamma = 0^\circ$ , and any low-lying  $K^\pi = 0^+$   
 897 states. The odd-spin states are not very sensitive to them 901  
 902 The quadrupole collective Hamiltonian approach can  
 predict a two-phonon  $\gamma$  vibrational band with  $K^\pi = 4^+$ ,



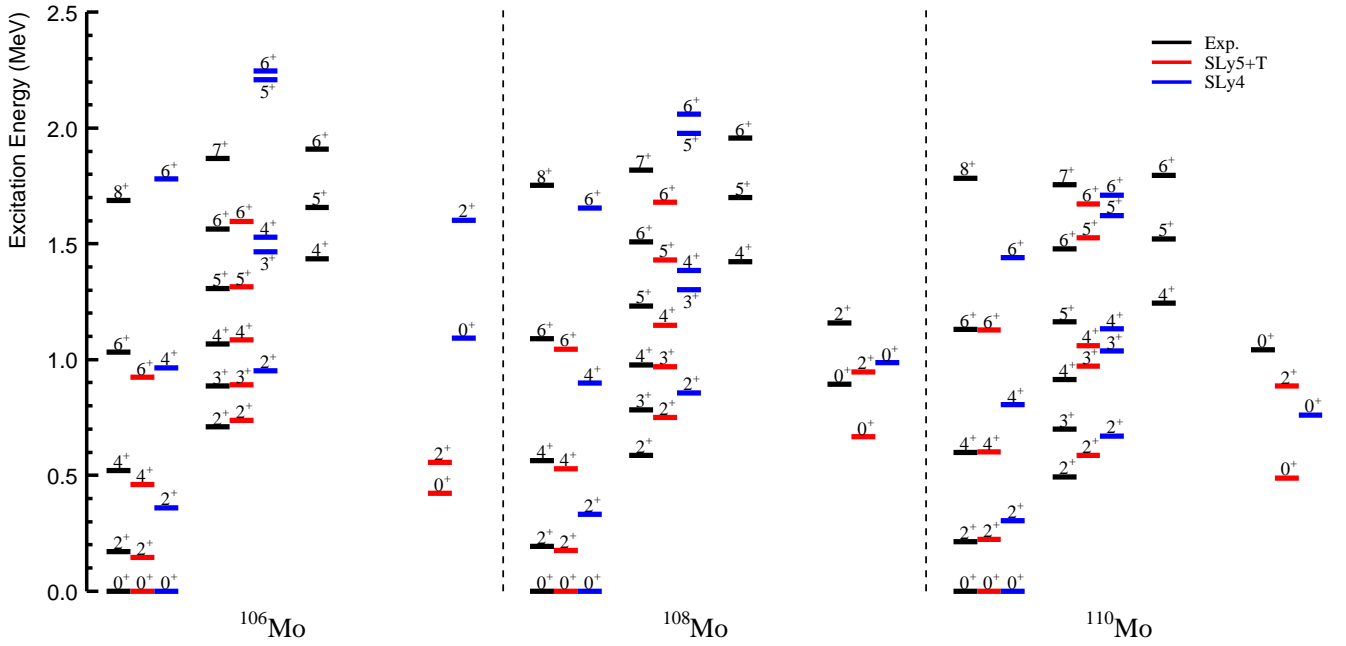


FIG. 17. The experimental and theoretical energies of the low-lying excited states in  $^{106}\text{Mo}$ ,  $^{108}\text{Mo}$ , and  $^{110}\text{Mo}$ . Black lines present the experimental results, and red and blue lines present the results from the theoretical calculations using SLy5+T and SLy4, respectively.

but not two quasiparticle states because it does not include the quasiparticle degrees of freedom explicitly. As discussed in Sec. IV C, the observed  $K^\pi = 4^+$  band is most likely built on a collective excitation. However, the  $K^\pi = 4^+$  band was not predicted by the calculations. An ideal two-phonon  $\gamma$  vibrational state has a wave function localized around the prolate minimum. To have a localized two-phonon  $K^\pi = 4^+$  vibrational state, which has a larger vibrational energy than that of a one-phonon state, generally the PES along the  $\gamma$  direction has to be deep enough to prevent oblate admixtures. If this is not satisfied, the corresponding two-phonon state will mix with the oblate shape and lose its two-phonon character. The potential barriers in the  $\gamma$  direction from the potential minimum, shown in Fig. 15, are shallow. By increasing in energy by 1 MeV or so from the prolate potential minimum, the other side of the axial symmetry at  $\gamma = 60^\circ$  (oblate) is reached. Further theoretical investigations are necessary to reproduce these collective excitations. One of the important improvements for the 5D collective model is to use effective interactions such as modern Skyrme energy density functionals instead of the P+Q Hamiltonian [62].

The squared wave functions of the  $0_2^+$  state in  $^{106,108,110}\text{Mo}$  with SLy5+T indicate  $\beta$  vibrational motion. On the other hand, the calculation with SLy4 indicates the possibility of shape coexistence of prolate and oblate shapes. Since the energy difference between the  $0_2^+$  and  $2_3^+$  states in  $^{108}\text{Mo}$  is consistent with the prediction with SLy5+T, the  $0_2^+$  state in  $^{108}\text{Mo}$  is suggested to be a  $\beta$  vibrational state. There is no experimental in-

formation providing a favored origin for the  $0_2^+$  state in  $^{110}\text{Mo}$ . Additional experimental and theoretical works are awaited for further discussions.

#### F. Structure of parent nuclei $^{106,108,110}\text{Nb}$

*Configuration of  $^{106}\text{Nb}$ :* The spin-parity of the  $\beta$ -decaying state in  $^{106}\text{Nb}$  was assigned to be  $4^-$ , and there were no experimental indications of the existence of a second  $\beta$ -decaying state. From the prompt  $\gamma$ -ray spectroscopy of the  $^{252}\text{Cf}$  spontaneous fission [63], the spin-parity of the ground state in  $^{106}\text{Nb}$  was assigned as  $1^-$ . Owing to the relatively strong population of high-spin states in  $^{106}\text{Mo}$  and the fact that no known  $\gamma$  rays of  $^{106}\text{Nb}$  are observed following the decay of  $^{106}\text{Zr}$ , it is likely that the  $\beta$ -decaying state of  $^{106}\text{Nb}$  is not the  $1^-$  ground state. The configuration of  $\pi 3/2^- [301] \otimes \nu 5/2^+ [413]$  with  $K^\pi = 1^-$  was proposed for the ground state [63]. In the Nilsson diagram [64], these quasiparticle states are predicted for the prolate shape with  $\beta \sim +0.35$  measured in  $^{106}\text{Mo}$ . The Gallagher-Moszkowski (GM) rule [65] predicts that the state with the antiparallel spin-coupling becomes a higher-lying state. Therefore, the observed  $\beta$ -decaying state was assigned to be a high-spin  $K^\pi = 4^-$  isomeric state of the GM partner in the  $\pi 3/2^- [301] \otimes \nu 5/2^+ [413]$  configuration.

*Configuration of  $^{108}\text{Nb}$ :* The spin-parity of the  $^{108}\text{Nb}$  ground-state was assigned to be  $2^-$ , and there was no evidence of a  $\beta$ -decaying isomeric state. The single-

TABLE VII. Candidates of the quasiparticle-state configurations of two  $\beta$ -decaying states in  $^{110}\text{Nb}$ . Four quasiparticle states are selected from the Nilsson diagram [64] and the quasiparticle level in the Woods-Saxon potential [66] for each nucleon. The left and right values show the spin-parity of the parallel- and antiparallel-spin coupling, respectively. The parallel-spin coupling state becomes lower-lying state [65]. The spins of the assigned configurations for the low and high-spin states are written in bold text.

	$\pi 1/2^+[431]$	$\pi 5/2^+[422]$	$\pi 5/2^-[303]$	$\pi 3/2^-[301]$
$\nu 5/2^+[402]$	$2^+/3^+$	$5^+/0^+$	$0^-/5^-$	$4^-/1^-$
$\nu 1/2^+[411]$	$1^+/0^+$	$2^+/3^+$	$3^-/2^-$	$1^-/2^-$
$\nu 7/2^-[523]$	$3^-/4^-$	<b><math>6^-/1^-</math></b>	$1^+/6^+$	$5^+/2^+$
$\nu 1/2^-[541]$	$1^-/0^-$	<b><math>2^-/3^-</math></b>	$3^+/2^+$	$1^+/2^+$

proton and neutron levels in the deformed nucleus were calculated according to the Nilsson diagram [64] and by using the Woods-Saxon potential [66]. A major difference of the level orderings between these two is the negative parity states of the protons. Candidates of the valence proton and neutron configurations were selected based on these two predictions. These are,  $\pi 1/2^+[431]$ ,  $\pi 5/2^+[422]$ ,  $\pi 5/2^-[303]$ , and  $\pi 3/2^-[301]$  for the proton configuration, and  $\nu 1/2^+[411]$ ,  $\nu 5/2^+[413]$ , and  $\nu 1/2^-[541]$  for the neutron configuration at around  $\beta = +0.33$  for  $^{108}\text{Mo}$ . The spin-parity of the  $\pi 5/2^-[303] \otimes \nu 1/2^+[411]$  configuration is  $2^-$  and  $3^-$  with the antiparallel- and parallel-spin couplings, respectively. The lower-lying state is the  $3^-$  state based on the GM rule. The  $2^-$  state would not form a  $\beta$ -decaying isomeric state because of a fast M1 transition to the  $3^-$  state. Thus, the expected  $\beta$ -decaying state is not the  $2^-$  state, but the  $3^-$  state. The  $2^-$  state of the  $\pi 3/2^-[301] \otimes \nu 1/2^+[411]$  configuration is also antiparallel-spin coupled, therefore the  $1^-$  state with the parallel-spin coupling would be the  $\beta$ -decaying state. The  $\pi 5/2^+[422] \otimes \nu 1/2^-[541]$  configuration can generate a  $\beta$ -decaying  $2^-$  state with the parallel-spin coupling. The  $3^-$  state with the antiparallel-spin coupling will decay to the  $2^-$  state by a M1 transition. Therefore, the ground state of  $^{108}\text{Nb}$  was assigned to be the  $2^-$  state with the  $\pi 5/2^+[422] \otimes \nu 1/2^-[541]$  configuration.

*Configuration of  $^{110}\text{Nb}$ :* Two  $\beta$ -decaying states were observed. The spin-parities were assigned to be  $2^-$  and  $6^-$ . The quasiparticle states are selected from the Nilsson diagram [64] at around  $\beta = +0.305$  for  $^{110}\text{Mo}$  or the single particle levels in the Woods-Saxon potential [66] as  $\pi 1/2^+[431]$ ,  $\pi 5/2^+[422]$ ,  $\pi 5/2^-[303]$ , and  $\pi 3/2^-[301]$  for the proton, and  $\nu 5/2^-[402]$ ,  $\nu 1/2^+[411]$ ,  $\nu 7/2^-[523]$ , and  $\nu 1/2^-[541]$  for the neutron. The spin-parities of the configuration coupled with these quasiparticle states are summarized in Table VII.

The  $6^-$  state is only generated by the parallel-spin coupling of the  $\pi 5/2^+[422] \otimes \nu 7/2^-[523]$  configuration. The anti-parallel spin coupled  $1^-$  state of this configuration, which has a higher energy based on the GM rule, would

not be a  $\beta$ -decaying state, because it can decay to the  $\beta$ -decaying  $2^-$  state by an M1 transition. For the low-spin  $2^-$  state, there are three candidates as given in Table VII. Since the spin difference between the GM pair is 1 for all three candidates, the lower energy state with the parallel spin becomes the  $\beta$ -decaying state. Thus, the parallel spin-coupling state of the  $\pi 5/2^+[422] \otimes \nu 1/2^-[541]$  configuration was assigned to the  $\beta$ -decaying  $2^-$  state.

The difference between the assigned configurations of the two  $\beta$ -decaying states is the neutron quasiparticle state. It is indicated that the  $\nu 7/2^-[523]$  and  $\nu 1/2^-[541]$  states are near the Fermi surface and close to each other. There was no experimental evidence to select the ground state from these two states.

*Comparison between Nilsson diagram and single-particle levels in Woods-Saxon potential:* The assigned configurations of  $^{106}\text{Nb}$ ,  $^{108}\text{Nb}$ , and  $^{110}\text{Nb}$  are consistent with the Nilsson diagram given in Ref. [64]. On the other hand, the  $\pi 5/2^+[422]$  state in the Woods-Saxon potential is located below  $Z = 40$  [66], even though it is used in the configuration of  $^{108}\text{Nb}$  and  $^{110}\text{Nb}$ . From comparison with the Nilsson diagram, it is suggested that the  $\pi 3/2^-[301]$  state in the Woods-Saxon potential may need to lower in energy so as to cross the  $\pi 5/2^+[422]$  state at  $\beta \sim 0.3$ .

## V. SUMMARY

The delayed  $\gamma$  rays emitted from the  $\beta$  decays of  $^{106,108,110}\text{Nb}$  were observed to investigate the shape evolution of  $^{106,108,110}\text{Mo}$ . The neutron-emission probability,  $P_n$ , of  $^{108}\text{Nb}$  and  $^{110}\text{Nb}$  was determined from the  $\beta$ -delayed  $\gamma$  rays emitted from the daughter nuclei with the same mass number. The daughter decays of  $^{106,108,110}\text{Zr}$  were used to search for  $\beta$ -decaying isomeric states in the Nb isotopes and to increase the statistics of the  $\gamma$  rays from  $^{106}\text{Mo}$  and  $^{108}\text{Mo}$ . Two  $\beta$ -decaying states with low and high spins were found in the  $^{110}\text{Nb}$   $\beta$  decay. Although the ground state in  $^{110}\text{Nb}$  was not assigned from these two candidates, the decay properties, including  $P_n$ , were separately determined for each state.

The lifetime of the  $2_1^+$  state in the Mo isotopes was measured by using the fast timing LaBr<sub>3</sub>(Ce) array. The quadrupole deformation parameter was obtained from the energy and lifetime of the  $2_1^+$  state. The deformation is almost unchanged with  $\beta \sim 0.33$  from the neutron number  $N = 62$  to  $66$  and slightly decreases to  $0.305(7)$  at  $N = 68$ . The even-odd energy staggering of the  $2_2^+$  band was evaluated using  $E_s(J)/E(2_1^+)$  as a function of the spin  $J$ . The staggering of the  $^{106}\text{Mo}$ ,  $^{108}\text{Mo}$ , and  $^{110}\text{Mo}$  isotopes shows the pattern of the  $\gamma$ -vibrational band. The comparison of kinematic moment of inertia between the ground and  $2_2^+$  bands supports the interpretation as the  $\gamma$ -vibrational band. A candidate of the two-phonon  $\gamma$  vibrational band was found well below the proton and neutron pairing gaps also in the  $^{110}\text{Mo}$  isotope.



The ground,  $\gamma$ , and two-phonon  $\gamma$  bands were compared to beyond-mean-field calculations. The ground-band energies and  $B(E2)$  of the  $2_1^+$  state were reproduced by the calculation with the SLy5+T interaction. The  $\gamma$  band of  $^{106}\text{Mo}$  was also reproduced very well. The comparison indicates that the shape is prolate with axial symmetry. However, the even-odd staggering of the  $\gamma$  band in  $^{110}\text{Mo}$  was not reproduced. The predicted potential might be too shallow toward the triaxial deformation especially for  $^{110}\text{Mo}$ . This may also be the reason why no two-phonon  $\gamma$  bands exist in the theoretical results.

The 893.4- and 1042.2-keV states in  $^{108}\text{Mo}$  and  $^{110}\text{Mo}$  were assigned as the second  $0^+$  states, respectively. On the other hand, the transition from the second  $0^+$  state previously reported in the  $\beta$ -decay to  $^{106}\text{Mo}$  was shown to be the known  $5_1^+ \rightarrow 4_1^+$  transition. The comparison with the beyond-mean-field calculation indicates a  $\beta$ -vibrational character for the  $0_2^+$  state in  $^{108}\text{Mo}$ .

The  $\log ft$  values were reasonably understood only when the first unique forbidden transition was introduced. It gave the strong constraint for the spin-parity assignment of the parent nuclei. The quasiparticle configurations of the parent nuclei were assigned by referring the Nilsson diagram for the prolate shape.

It is interesting to investigate whether the disagreement between the experiment and prediction for  $^{110}\text{Mo}$  is enhanced at heavier Mo isotopes or not. The low-lying  $2_1^+$ ,  $4_1^+$ , and  $2_2^+$  states are known in  $^{112}\text{Mo}$  [16]. In order to study the triaxial motion, measurements of the higher spin states in the  $2_2^+$  band are awaited.

## ACKNOWLEDGEMENTS

We would like to express our gratitude to the RIKEN Nishina Center accelerator staff for providing a stable and high intensity  $^{238}\text{U}$  primary beam. This work was supported by JSPS KAKENHI Grants Nos. 24740188, 25247045, 26800117, and 16K17680, NRF Grant No. 2016K1A3A7A09005575, STFC Grant Nos. ST/J000132/1, ST/J000051/1 and ST/K502431/1, DOE Grant No. DE-FG02-91ER-40609, and Spanish Ministerio de Ciencia e Innovación under Contracts No. FPA2009-13377-C02 and No. FPA2011-29854-C04. P.H.R. acknowledges support from the UK National Measurement Office (NMO). P.-A.S. was financed by JSPS Grant No. 23 01752 and the RIKEN Foreign Postdoctoral Researcher Program. We acknowledge the EUROBALL Owners Committee for the loan of germanium detectors and the PreSpec Collaboration for the readout electronics of the cluster detectors. NH acknowledges the JSPS-NSFC Bilateral Program for the Joint Research Project on "Nuclear mass and life for unravelling mysteries of r-process." Numerical calculations were performed in part using the COMA (PACS-IX) and Oakforest-PACS provided by Multidisciplinary Cooperative Research Program in Center for Computational Sciences, University of Tsukuba.

- 
- [1] R. F. Casten, *Nuclear Structure from a Simple Perspective* (Oxford University Press, Oxford, 2000).
- [2] A. S. Davydov and G. F. Filippov, Nucl. Phys. **8**, 237 (1958).
- [3] L. Wilets and M. Jean, Phys. Rev. **102**, 788 (1956).
- [4] M. A. Caprio, Phys. Rev. C **83**, 064309 (2011).
- [5] J. Skalski, S. Mizutori, and W. Nazarewicz, Nucl. Phys. A **617**, 282 (1997).
- [6] S. Hilaire and M. Girod, AIP Conference Proceedings **1012**, 359 (2008). [http://www-phynu.cea.fr/science\\_en\\_ligne/carte\\_potentiels\\_microscopiques/carte\\_potentiel\\_nucleaire\\_eng.htm](http://www-phynu.cea.fr/science_en_ligne/carte_potentiels_microscopiques/carte_potentiel_nucleaire_eng.htm).
- [7] C. L. Zhang, G. H. Bhat, W. Nazarewicz, J. A. Sheikh, and Y. Shi, Phys. Rev. C **92**, 034307 (2015).
- [8] A.-C. Dai, F.-R. Xu, and W.-Y. Liang, Chinese Physics C **43**, 084101 (2019).
- [9] D. Ralet, S. Pietri, T. Rodríguez, M. Alaqeel, T. Alexander, N. Alkhomashi, F. Ameil, T. Arici, A. Ataç, R. Avigo, T. Bäck, D. Bazzacco, B. Birkenbach, P. Boutachkov, B. Bruyneel, A. M. Bruce, F. Camera, B. Cederwall, S. Ceruti, E. Clément, M. L. Cortés, D. Curien, G. De Angelis, P. Désesquelles, M. Dewald, F. Didierjean, C. Domingo-Pardo, M. Doncel, G. Duchêne, J. Eberth, A. Gadea, J. Gerl, F. Ghazi Moradi, H. Geissel, T. Goigoux, N. Goel, P. Golubev, V. González, M. Górska, A. Gottardo, E. Gregor, G. Guastalla, A. Givchev, T. Habermann, M. Hackstein, L. Harkness-Brennan, G. Henning, H. Hess, T. Hüyük, J. Jolie, D. S. Judson, A. Jungclaus, R. Knoebel, I. Kojouharov, A. Korichi, W. Korten, N. Kurz, M. Labiche, N. Lalović, C. Louchart-Henning, D. Mengoni, E. Merchán, B. Million, A. I. Morales, D. Napoli, F. Naqvi, J. Nyberg, N. Pietralla, Z. Podolyák, A. Pulia, A. Prochazka, B. Quintana, G. Rainovski, M. Reese, F. Recchia, P. Reiter, D. Rudolph, M. D. Salsac, E. Sanchis, L. G. Sarmiento, H. Schaffner, C. Scheidenberger, L. Sengele, B. S. N. Singh, P. P. Singh, C. Stahl, O. Stezowski, P. Thoele, J. J. Valiente Dobon, H. Weick, A. Wendt, O. Wieland, J. S. Winfield, H. J. Wollersheim, and M. Zielinska (for the PreSPEC and PreSPEC and AGATA Collaborations), Phys. Rev. C **95**, 034320 (2017).
- [10] H. Ahrens, N. Kaffrell, N. Trautmann, and G. Herrmann, Phys. Rev. C **14**, 211 (1976).
- [11] B. D. Kern, K. Sistemich, W.-D. Lauppe, and H. Lawin, Z. Phys. A **306**, 161 (1982).
- [12] K. Shizuma, H. Lawin, and K. Sistemich, Z. Phys. A **311**, 71 (1983).
- [13] A. Guessous, N. Schulz, W. R. Phillips, I. Ahmad, M. Bentaleb, J. L. Durell, M. A. Jones, M. Leddy, E. Lubkiewicz, L. R. Morss, R. Piepenbring, A. G. Smith, W. Urban, and B. J. Varley, Phys. Rev. Lett. **75**, 2280 (1995).

- [14] A. Guessous, N. Schulz, M. Bentaleb, E. Lubkiewicz, J. L. Durell, C. J. Pearson, W. R. Phillips, J. A. Shanon, W. Urban, B. J. Varley, I. Ahmad, C. J. Lister, L. R. Morss, K. L. Nash, C. W. Williams, and S. Khazrouni, *Phys. Rev. C* **53**, 1191 (1996).
- [15] H. Watanabe, K. Yamaguchi, A. Odahara, T. Sumikama, S. Nishimura, K. Yoshinaga, Z. Li, Y. Miyashita, K. Sato, L. Próchniak, H. Baba, J. S. Berryman, N. Blasi, A. Bracco, F. Camera, J. Chiba, P. Doornenbal, S. Go, T. Hashimoto, S. Hayakawa, C. Hinke, N. Hinohara, E. Ideguchi, T. Isobe, Y. Ito, D. G. Jenkins, Y. Kawada, N. Kobayashi, Y. Kondo, R. Krücken, S. Kubono, G. Lorusso, T. Nakano, T. Nakatsukasa, M. Kurata-Nishimura, H. J. Ong, S. Ota, Z. Podolyák, H. Sakurai, H. Scheit, K. Steiger, D. Steppenbeck, K. Sugimoto, K. Tajiri, S. Takano, A. Takashima, T. Teranishi, Y. Wakabayashi, P. M. Walker, O. Wieland, and H. Yamaguchi, *Phys. Lett. B* **704**, 270 (2011).
- [16] N. Paul, A. Corsi, A. Obertelli, P. Doornenbal, G. Authalet, H. Baba, B. Bally, M. Bender, D. Calvet, F. Château, S. Chen, J.-P. Delaroche, A. Delbart, J.-M. Gheller, A. Giganon, A. Gillibert, M. Girod, P.-H. Heenen, V. Lapoux, J. Libert, T. Motobayashi, M. Niikura, T. Otsuka, T. R. Rodríguez, J.-Y. Roussé, H. Sakurai, C. Santamaria, N. Shimizu, D. Steppenbeck, R. Taniuchi, T. Togashi, Y. Tsumoda, T. Uesaka, T. Ando, T. Arici, A. Blazhev, F. Browne, A. M. Bruce, R. Carroll, L. X. Chung, M. L. Cortés, M. Dewald, B. Ding, F. Flayigny, S. Franchoo, M. Górski, A. Gottardo, A. Jungclauss, J. Lee, M. Lettmann, B. D. Linh, J. Liu, Z. Liu, C. Lizarazo, S. Momiyama, K. Moschner, S. Nagamine, N. Nakatsuka, C. Nita, C. R. Nobs, L. Olivier, Z. Patel, Z. Podolyák, M. Rudigier, T. Saito, C. Shand, P.-A. Söderström, I. Stefan, R. Orlandi, V. Vaquero, V. Werner, K. Wimmer, and Z. Xu, *Phys. Rev. Lett.* **118**, 032501 (2017).
- [17] N. V. Zamfir and R. F. Casten, *Phys. Lett. B* **260**, 265 (1991).
- [18] R. Casten, E. Flynn, O. Hansen, and T. Mulligan, *Nucl. Phys. A* **184**, 357 (1972).
- [19] S. Takeda, S. Yamaji, K. Matsuda, I. Kohno, N. Nakanishi, Y. Aways, and S. Kusuno, *J. Phys. Soc. Jpn.* **34**, 1115 (1973), <https://doi.org/10.1143/JPSJ.34.1115>.
- [20] K. Sistemich, W. D. Lauppe, H. Lawin, H. Seyfarth, and B. D. Kern, *Z. Phys. A* **289**, 225 (1979).
- [21] H. Penttilä, P. Dendooven, A. Honkanen, M. Huhta, G. Lhersonneau, M. Oinonen, J.-M. Parmonen, K. Peräjärvi, J. Äystö, J. Kurpeta, and J. R. Persson, *Phys. Rev. C* **54**, 2760 (1996).
- [22] F. Browne, A. M. Bruce, T. Sumikama, I. Nishizuka, S. Nishimura, P. Doornenbal, G. Lorusso, Z. Patel, S. Rice, L. Sinclair, P.-A. Söderström, H. Watanabe, J. Wu, Z. Y. Xu, H. Baba, N. Chiga, R. Carroll, R. Daido, F. Didierjean, Y. Fang, G. Gey, E. Ideguchi, N. Inabe, T. Isobe, D. Kameda, I. Kojouharov, N. Kurz, T. Kubo, S. Lalkovski, Z. Li, R. Lozeva, N. Naoki, H. Nishibata, A. Odahara, Z. Podolyák, P. H. Regan, O. J. Roberts, H. Sakurai, H. Schaffner, G. S. Simpson, H. Suzuki, H. Takeda, M. Tanaka, J. Taprogge, V. Werner, O. Wieland, and A. Yagi, *Acta Phys. Pol. B* **46**, 721 (2015).
- [23] T. Kubo, *Nucl. Instrum. Methods B* **204**, 97 (2003).
- [24] T. Kubo, D. Kameda, H. Suzuki, N. Fukuda, H. Takeda, Y. Yanagisawa, M. Ohtake, K. Kusaka, K. Yoshida, N. Inabe, T. Ohnishi, A. Yoshida, K. Tanaka, and Y. Mizoi, *Prog. Theor. Exp. Phys.* **2012**, 03C003 (2012).
- [25] T. Sumikama, F. Browne, A. M. Bruce, I. Nishizuka, S. Nishimura, P. Doornenbal, G. Lorusso, Z. Patel, S. Rice, L. Sinclair, P.-A. Söderström, H. Watanabe, J. Wu, Z. Y. Xu, A. Yagi, H. Baba, N. Chiga, R. Carroll, R. Daido, F. Didierjean, Y. Fang, G. Gey, E. Ideguchi, N. Inabe, T. Isobe, D. Kameda, I. Kojouharov, N. Kurz, T. Kubo, S. Lalkovski, Z. Li, R. Lozeva, N. Fukuda, H. Nishibata, A. Odahara, Z. Podolyák, P. H. Regan, O. J. Roberts, H. Sakurai, H. Schaffner, G. S. Simpson, H. Suzuki, H. Takeda, M. Tanaka, J. Taprogge, V. Werner, and O. Wieland, *RIKEN Accel. Prog. Rep.* **47**, 9 (2014).
- [26] S. Nishimura, *Prog. Theor. Exp. Phys.* **2012**, 03C006 (2012).
- [27] S. Nishimura, G. Lorusso, Z. Xu, J. Wu, R. Gernhäuser, H. Jung, Y. Kwon, Z. Li, K. Steiger, and H. Sakurai, *RIKEN Accel. Prog. Rep.* **46**, 182 (2013).
- [28] I. Nishizuka, T. Sumikama, F. Browne, A. M. Bruce, S. Nishimura, P. Doornenbal, G. Lorusso, Z. Patel, S. Rice, L. Sinclair, P.-A. Söderström, H. Watanabe, J. Wu, Z. Y. Xu, A. Yagi, H. Baba, N. Chiga, R. Carroll, R. Daido, F. Didierjean, Y. Fang, N. Fukuda, G. Gey, E. Ideguchi, N. Inabe, T. Isobe, D. Kameda, I. Kojouharov, N. Kurz, T. Kubo, S. Lalkovski, Z. Li, R. Lozeva, H. Nishibata, A. Odahara, Z. Podolyák, P. H. Regan, O. J. Roberts, H. Sakurai, H. Schaffner, G. S. Simpson, H. Suzuki, H. Takeda, M. Tanaka, J. Taprogge, V. Werner, and O. Wieland, *JPS Conf. Proc.* **6**, 030062 (2015).
- [29] J. Ha, T. Sumikama, and S. Choi, *Nucl. Instrum. Methods B* **463**, 216 (2020).
- [30] P.-A. Söderström, S. Nishimura, P. Doornenbal, G. Lorusso, T. Sumikama, H. Watanabe, Z. Y. Xu, H. Baba, F. Browne, S. Go, G. Gey, T. Isobe, H.-S. Jung, G. D. Kim, Y.-K. Kim, I. Kojouharov, N. Kurz, Y. K. Kwon, Z. Li, K. Moschner, T. Nakao, H. Nishibata, M. Nishimura, A. Odahara, H. Sakurai, H. Schaffner, T. Shimoda, J. Taprogge, Z. Vajta, V. Werner, J. Wu, A. Yagi, and K. Yoshinaga, *Nucl. Instrum. Methods B* **317**, 649 (2013).
- [31] Z. Patel, F. Browne, A. M. Bruce, N. Chiga, R. Daido, S. Nishimura, Z. Podolyák, P. H. Regan, O. J. Roberts, H. Sakurai, P.-A. Söderström, T. Sumikama, and H. Watanabe, *RIKEN Accel. Prog. Rep.* **47**, 13 (2014).
- [32] J. C. Hill, D. D. Schwellenbach, F. K. Wohn, J. A. Winger, R. L. Gill, H. Ohm, and K. Sistemich, *Phys. Rev. C* **43**, 2591 (1991).
- [33] M. Wang, G. Audi, F. G. Kondev, W. J. Huang, S. Naimi, and X. Xu, *Chin. Phys. C* **41**, 030003 (2017).
- [34] ENSDF database, <http://www.nndc.bnl.gov/ensdf>.
- [35] X. Rui-Qing, Z. Sheng-Jiang, J. H. Hamilton, A. V. Ramayya, J. K. Hwang, X. Q. Zhang, L. Ke, Y. Li-Ming, Z. Ling-Yan, G. Cui-Yun, Z. Zheng, J. Zhuo, X. Shu-Dong, W. C. Ma, J. Kormicki, E. F. Jones, J. D. Cole, R. Aryaeinejad, M. W. Drigert, I. Y. Lee, J. O. Rasmussen, M. A. Stoyer, G. M. Ter-Akopian, and A. V. Daniel, *Chin. Phys. Lett.* **19**, 180 (2002).
- [36] S. J. Zhu, J. H. Hamilton, A. V. Ramayya, P. M. Gore, J. O. Rasmussen, V. Dimitrov, S. Frauendorf, R. Q. Xu, J. K. Hwang, D. Fong, L. M. Yang, K. Li, Y. J. Chen, X. Q. Zhang, E. F. Jones, Y. X. Luo, I. Y. Lee, W. C. Ma, J. D. Cole, M. W. Drigert, M. Stoyer, G. M. Ter-Akopian,

- and A. V. Daniel, Eur. Phys. J. A **25**, 459 (2005).
- [37] E. F. Jones, P. M. Gore, S. J. Zhu, J. H. Hamilton, A. V. Ramayya, J. K. Hwang, R. Q. Xu, L. M. Yang, K. Li, Z. Jiang, Z. Zhang, S. D. Xiao, X. Q. Zhang, W. C. Ma, J. D. Cole, M. W. Drigert, I. Y. Lee, J. O. Rasmussen, Y. X. Luo, and M. A. Stoyer, Phys. Atom. Nucl. **69**, 1198 (2006).
- [38] Calculation program of *logft*, <http://www.nndc.bnl.gov/logft>.
- [39] T. Kibédi, T. W. Burrows, M. B. Trzhaskovskaya, P. M. Davidson, and C. W. Nestor Jr, Nucl. Instrum. Methods A **589**, 202 (2008).
- [40] B. Singh, J. L. Rodriguez, S. S. M. Wong, and J. K. Tuli, Nucl. Data Sheets **84**, 487 (1998).
- [41] H. Behrens and W. Bühring, *Electron Radial Wave Functions and Nuclear Beta-decay* (Oxford Science Publications, 1982).
- [42] J. A. Pinston, W. Urban, C. Droste, T. Rzača-Urban, J. Genevey, G. Simpson, J. L. Durell, A. G. Smith, B. J. Varley, and I. Ahmad, Phys. Rev. C **74**, 064304 (2006).
- [43] T. Mehren, B. Pfeiffer, S. Schoedder, K.-L. Kratz, M. Huhta, P. Dendooven, A. Honkanen, G. Lhersonneau, M. Oinonen, J.-M. Parmonen, H. Penttilä, A. Popov, V. Rubchenya, and J. Äystö, Phys. Rev. Lett. **77**, 458 (1996).
- [44] J. Pereira, S. Hennrich, A. Aprahamian, O. Arndt, A. Becerril, T. Elliot, A. Estrade, D. Galaviz, R. Kessler, K.-L. Kratz, G. Lorusso, P. F. Mantica, M. Matos, P. Möller, F. Montes, B. Pfeiffer, H. Schatz, F. Schertz, L. Schnorrenberger, E. Smith, A. Stolz, M. Quinn, W. B. Walters, and A. Wöhr, Phys. Rev. C **79**, 035806 (2009).
- [45] W. Urban, T. Rzača-Urban, J. L. Durell, W. R. Phillips, A. G. Smith, B. J. Varley, I. Ahmad, and N. Schulz, Eur. Phys. J. A **20**, 381 (2004).
- [46] G. Lorusso, S. Nishimura, Z. Y. Xu, A. Jungclaus, Y. Shimizu, G. S. Simpson, P.-A. Söderström, H. Watanabe, F. Browne, P. Doornenbal, G. Gey, H. S. Jung, B. Meyer, T. Sumikama, J. Taprogge, Z. Vajta, J. Wu, H. Baba, G. Benzoni, K. Y. Chae, F. C. L. Crespi, N. Fukuda, R. Gernhäuser, N. Inabe, T. Kajino, D. Kameda, G. D. Kim, Y.-K. Kim, I. Kojouharov, F. G. Kondev, T. Kubo, N. Kurz, Y. K. Kwon, G. J. Lane, Z. Li, A. Montaner-Pizá, K. Moschner, F. Naqvi, M. Niikura, H. Nishibata, A. Odahara, R. Orlandi, Z. Patel, Z. Podolyák, H. Sakurai, H. Schaffner, P. Schury, S. Shibagaki, K. Steiger, H. Suzuki, H. Takeda, A. Wendt, A. Yagi, and K. Yoshinaga, Phys. Rev. Lett. **114**, 192501 (2015).
- [47] G. Mamane, Ph.D. thesis, Weizmann Inst.Science, Rehovot (1983).
- [48] B. Pritychenko, M. Birch, B. Singh, and M. Horoi, At. Data Nucl. Data Tables **107**, 1 (2016).
- [49] E. Cheifetz, R. C. Jared, S. G. Thompson, and J. B. Wilhelmy, Phys. Rev. Lett. **25**, 38 (1970).
- [50] J. K. Hwang, A. V. Ramayya, J. H. Hamilton, Y. X. Luo, A. V. Daniel, G. M. Ter-Akopian, J. D. Cole, and S. J. Zhu, Phys. Rev. C **73**, 044316 (2006).
- [51] E. Cheifetz, H. Selic, A. Wolf, R. Chechik, and J. Wilhelmy, in *Proc. Conf. Nucl. Spectr. Fission Products* (1980) p. 193.
- [52] S. Raman, C. W. Nestor Jr, and P. Tikkanen, At. Data Nucl. Data Tables **78**, 1 (2001).
- [53] F. Browne, A. M. Bruce, T. Sumikama, I. Nishizuka, S. Nishimura, P. Doornenbal, G. Lorusso, P.-A. Söderström, H. Watanabe, R. Daido, Z. Patel, S. Rice, L. Sinclair, J. Wu, Z. Y. Xu, A. Yagi, H. Baba, N. Chiga, R. Carroll, F. Didierjean, Y. Fang, N. Fukuda, G. Gey, E. Ideguchi, N. Inabe, T. Isobe, D. Kameda, I. Kojouharov, N. Kurz, T. Kubo, S. Lalkovski, Z. Li, R. Lozeva, H. Nishibata, A. Odahara, Z. Podolyák, P. H. Regan, O. J. Roberts, H. Sakurai, H. Schaffner, G. S. Simpson, H. Suzuki, H. Takeda, M. Tanaka, J. Taprogge, V. Werner, and O. Wieland, Phys. Lett. B **750**, 448 (2015).
- [54] S. Ansari, J.-M. Régis, J. Jolie, N. Saed-Samii, N. Warr, W. Korten, M. Zielińska, M.-D. Salsac, A. Blanc, M. Jentschel, U. Köster, P. Mutti, T. Soldner, G. S. Simpson, F. Drouet, A. Vancraeynest, G. de France, E. Clément, O. Stezowski, C. A. Ur, W. Urban, P. H. Regan, Z. Podolyák, C. Larijani, C. Townsley, R. Carroll, E. Wilson, H. Mach, L. M. Fraile, V. Pazi, B. Olaizola, V. Vedia, A. M. Bruce, O. J. Roberts, J. F. Smith, M. Scheck, T. Kröll, A.-L. Hartig, A. Ignatov, S. Ilieva, S. Lalkovski, N. Mărginean, T. Otsuka, N. Shimizu, T. Togashi, and Y. Tsunoda, Phys. Rev. C **96**, 054323 (2017).
- [55] G. Alaga, K. Alder, A. Bohr, and B. R. Mottelson, Mat. Fys. Medd. K. Dan. Vidensk. Selsk. **29** (1955).
- [56] J. M. Eldridge, B. Fenker, J. H. Hamilton, C. Goodin, C. J. Zachary, E. Wang, A. V. Ramayya, A. V. Daniel, G. M. Ter-Akopian, Y. T. Oganessian, Y. X. Luo, J. O. Rasmussen, and S. J. Zhu, Eur. Phys. J. A **54**, 15 (2018).
- [57] P.-A. Söderström, G. Lorusso, H. Watanabe, S. Nishimura, P. Doornenbal, G. Thiamova, F. Browne, G. Gey, H. S. Jung, T. Sumikama, J. Taprogge, Z. Vajta, J. Wu, Z. Y. Xu, H. Baba, G. Benzoni, K. Y. Chae, F. C. L. Crespi, N. Fukuda, R. Gernhäuser, N. Inabe, T. Isobe, A. Jungclaus, D. Kameda, G. D. Kim, Y.-K. Kim, I. Kojouharov, F. G. Kondev, T. Kubo, N. Kurz, Y. K. Kwon, G. J. Lane, Z. Li, A. Montaner-Pizá, K. Moschner, F. Naqvi, M. Niikura, H. Nishibata, A. Odahara, R. Orlandi, Z. Patel, Z. Podolyák, H. Sakurai, H. Schaffner, G. S. Simpson, K. Steiger, H. Suzuki, H. Takeda, A. Wendt, A. Yagi, and K. Yoshinaga, Phys. Rev. C **88**, 024301 (2013).
- [58] N. Hinohara, K. Sato, T. Nakatsukasa, M. Matsuo, and K. Matsuyanagi, Phys. Rev. C **82**, 064313 (2010).
- [59] N. Hinohara, K. Sato, K. Yoshida, T. Nakatsukasa, M. Matsuo, and K. Matsuyanagi, Phys. Rev. C **84**, 061302(R) (2011).
- [60] K. Sato, N. Hinohara, K. Yoshida, T. Nakatsukasa, M. Matsuo, and K. Matsuyanagi, Phys. Rev. C **86**, 024316 (2012).
- [61] T. Sumikama, K. Yoshinaga, H. Watanabe, S. Nishimura, Y. Miyashita, K. Yamaguchi, K. Sugimoto, J. Chiba, Z. Li, H. Baba, J. S. Berryman, N. Blasi, A. Bracco, F. Camera, P. Doornenbal, S. Go, T. Hashimoto, S. Hayakawa, C. Hinke, E. Ideguchi, T. Isobe, Y. Ito, D. G. Jenkins, Y. Kawada, N. Kobayashi, Y. Kondo, R. Krücken, S. Kubono, G. Lorusso, T. Nakano, M. Kurata-Nishimura, A. Odahara, H. J. Ong, S. Ota, Z. Podolyák, H. Sakurai, H. Scheit, K. Steiger, D. Steffenbeck, S. Takano, A. Takashima, K. Tajiri, T. Teranishi, Y. Wakabayashi, P. M. Walker, O. Wieland, and H. Yamaguchi, Phys. Rev. Lett. **106**, 202501 (2011).
- [62] K. Washiyama and T. Nakatsukasa, Phys. Rev. C **96**, 041304(R) (2017).

- [63] Y. X. Luo, J. O. Rasmussen, J. H. Hamilton, A. V. Rasmussen, E. Wang, Y. X. Liu, C. F. Jiao, W. Y. Liang, F. R. Xu, Y. Sun, S. Frauendorf, J. K. Hwang, S. H. Liu, S. J. Zhu, N. T. Brewer, I. Y. Lee, G. M. Ter-Akopian, Y. Oganessian, R. Donangelo, and W. C. Ma, Phys. Rev. C **89**, 044326 (2014).
- [64] Y.-X. Liu, Y. Sun, X.-H. Zhou, Y.-H. Zhang, S.-Y. Yu, Y.-C. Yang, and H. Jin, Nucl. Phys. A **858**, 11 (2011).
- [65] C. J. Gallagher Jr and S. A. Moszkowski, Phys. Rev. **111**, 1282 (1958).
- [66] F. R. Xu, P. M. Walker, and R. Wyss, Phys. Rev. C **65**, 021303(R) (2002).